NUCL SCI TECH (2021) 32:24
https://doi.org/10.1007/s41365-021-00862-6

Low-energy X-ray attenuation characteristics of *Rhizophora* spp. composites

Damilola Oluwafemi Samson[1,3] · Ahmad Shukri[1] · Mohd Zubir Mat Jafri[1] · Rokiah Hashim[2] · Mohd Zahri Abdul Aziz[3] · Sylvester Jande Gemanam[1] · Mohd Fahmi Mohd Yusof[4]

Received: 27 October 2020 / Revised: 5 January 2021 / Accepted: 13 January 2021 / Published online: 14 March 2021

Abstract Photon absorption parameters such as mass attenuation coefficients (μ_m), molar extinction coefficients (ε), total molecular ($\sigma_{t,m}$), atomic ($\sigma_{t,a}$) and electronic ($\sigma_{t,el}$) cross sections, half-value layers ($X_{1/2}$), tenth-value layers ($X_{1/10}$), mean free paths (λ), effective atomic numbers (Z_{eff}), and effective electron densities (N_{el}) were estimated for defatted soy flour (DSF), soy protein concentrate (SPC), and soy protein isolate (SPI)-based *Rhizophora* spp. particleboard composites substituted with 10 wt% sodium hydroxide (NaOH) and 0, 5, 10, and 15 wt% itaconic acid polyamidoamine-epichlorohydrin (IA-PAE) adhesives. Elemental composition was assessed using ultrahigh-resolution field emission scanning electron microscopy-energy dispersive X-ray spectrometry (UHR-FESEM-EDX). The interaction parameters were evaluated for $K_{\alpha 1}$ photons at 16.59, 17.46, 21.21, and 25.26 keV, employing a low-energy germanium (LEGe) detector system and an ^{241}Am γ-ray source. X-ray diffraction characterization revealed an amorphous phase in the developed particleboard composites. Samples DSF15′, SPC15′, and SPI15′ exhibited the highest values of μ_m, ε, $\sigma_{t,m}$, Z_{eff}, and N_{el} among all of the studied particleboard samples, within the range of measured photon energies. In addition, all of the modified samples exhibited lower $X_{1/2}$, $X_{1/10}$, λ, $\sigma_{t,a}$, and $\sigma_{t,el}$ than the unmodified samples, with DSF-, SPC-, and SPI/NaOH/*Rhizophora* spp./IA-PAE (15 wt%), indicating insignificant changes. The current results of the particleboard samples' analysis can be useful for medical radiation applications and shielding research.

Keywords Photon interaction parameters · Shielding · DSF–SPC–SPI · Particleboards · NaOH/IA-PAE

1 Introduction

In the fabrication of radiological safety materials, significant attention has been paid to the use of heavy elements, including lead (Pb), tungsten (W), iron (Fe), or mixtures of these substances, and various concrete-based radiation shields [1, 2]. However, much concern has been expressed about the environmental health issues associated with the use of materials made of Pb and Pb-based compounds. The disadvantages include inflexibility, chemical instability, poor physico-mechanical strength and dimensional stability, weight, and the nature of toxicity [3]. Lead dust can become airborne and may be ingested by humans [4]. It is not easily excreted from the human body, nor is it biodegradable or biocompatible. The ultimate concern is that of the failure of multiple organs. On the other hand, there are various challenges related to the use of concrete-

This work was supported by the Universiti Sains Malaysia (USM), from the Research University Grant allocation (Nos. 304/PFIZIK/6316173, 1001/PFIZIK/822173, 203/PTEKIND/6711525).

✉ Damilola Oluwafemi Samson
saamdoftt82@gmail.com

✉ Mohd Zubir Mat Jafri
mjafri@usm.my

[1] School of Physics, Universiti Sains Malaysia, 11800 Gelugor, Penang, Malaysia

[2] School of Industrial Technology, Universiti Sains Malaysia, 11800 Gelugor, Penang, Malaysia

[3] Advanced Medical and Dental Institute, Universiti Sains Malaysia, 13200 Bertam, Penang, Malaysia

[4] School of Health Sciences, Universiti Sains Malaysia, 16150 Kota Bharu, Kelantan, Malaysia

based materials, arising, e.g., when concrete is heated owing to the radiation energy absorption, which leads to the loss of water and induces significant variability in the concrete chemical composition, deterioration of structural strength, and reduction in its density. In general, materials must have high atomic numbers and should be sufficiently homogeneous in terms of their density and chemical composition to be applicable for radiation shielding. Therefore, in recent years, the evaluation of specific values of interacting factors of composite materials has been of significant experimental and theoretical interest [5]. Several researchers have adopted various natural (renewables) or synthetic (petroleum-based) composite materials to create novel radiation shielding materials, for substituting lead-containing shields using different techniques [5–7]. Owing to their specific characteristics, such as homogeneity, wide range of elemental compositions, non-toxicity, ease of fabrication in different shapes and sizes with no discrepancy in their density, high flexibility, and convenient attenuation coefficients, renewable resources such as wood composites can be used in radiation shielding materials [8, 9].

Rhizophora spp. (*Rh.* spp.) wood is particularly interesting owing to its unique physico-mechanical and dimensional stability characteristics, and it has found applications in radiation dosimetry [8–10]. Typical *Rh.* spp. wood, with high carbon content followed by oxygen, hydrogen, and other elements, is suitable for use as a particleboard radiation shielding material [5, 9, 11]. Untreated *Rh.* spp. wood, however, has some drawbacks if it is utilized for radiation protection against ionizing radiation [9, 12]. In several studies, an addition of suitable curing agent has been considered, which may enhance the physico-mechanical and radiation shielding characteristics of *Rh.* spp. [8, 10].

The demand for soy protein-based (defatted soy flour (DSF), soy protein concentrate (SPC), and soy protein isolate (SPI)) materials for various medical health applications continues to increase owing to their advantageous characteristics, such as biodegradability, biocompatibility, and cost-effectiveness [8, 13]. Soy protein composites have been noted for their strong network, high thermal stability, advantageous physico-mechanical parameters, high chemical durability, and good dimensional stability. A recent trend has been to incorporate network modifiers like sodium hydroxide (NaOH) or itaconic acid polyamidoamine-epichlorohydrin (IA-PAE) resin, for overcoming disadvantages such as poor water resistance, high viscosity, low solid content, and low effective atomic number, exhibited by unmodified soy protein composites [8, 14, 15]. NaOH has been recognized as an important denaturing agent that unfurls protein molecules to expose hydrophobic groups, which helps in strengthening the adhesive physico-mechanical characteristics and wood-bonding ability [15]. However, NaOH alone does not provide convenient modifier specifications for photon absorption parameters and requires at least one curing agent, such as IA-PAE resin. IA-PAE, which can be produced from sugars, is a non-toxic compound and is considered one of the most useful building block chemicals with incomparable multifunctionality. In view of this, the combination of DSF, SPC, SPI, and NaOH/IA-PAE adhesives in terms of shielding X- and γ-rays can constitute a novel and alternative candidate material.

Therefore, in the present study, the radiation interaction properties of uncured and cured DSF-, SPC-, and SPI/NaOH/IA-PAE/*Rh.* spp. particleboards encoded as DSF0, SPC0, SPI0, DSF1, SPC1, SPI1, DSF5, SPC5, SPI5, DSF10, SPC10, SPI10, DSF15, SPC15, SPI15, DSF5′, SPC5′, SPI5′, DSF10′, SPC10′, SPI10′, DSF15′, SPC15′, and SPI15′ for 0, 5, 10, and 15 wt% were experimentally determined for 16.59, 17.46, 21.21, and 25.26 keV photons. Crucial radiation interaction parameters, such as mass attenuation coefficients (μ_m), molar extinction coefficients (ε), total molecular ($\sigma_{t,m}$), atomic ($\sigma_{t,a}$) and electronic ($\sigma_{t,el}$) cross sections, half-value layer (HVL) values ($X_{1/2}$), tenth-value layer (TVL) values ($X_{1/10}$), mean free path (MFP) values (λ), effective atomic numbers (Z_{eff}), and effective electron densities (N_{el}) were evaluated to provide accurate information on the performance of the photon radiation shielding characteristics of various soy protein-based adhesives used in the fields of medical diagnostics and radiation dosimetry.

2 Materials and methods

2.1 Fabrication of DSF-, SPC-, and SPI/NaOH/IA-PAE/*Rh.* spp. particleboard samples

Rh. spp. trunks, obtained from the Forestry Department of the Mangrove Forest Reserve in Kuala Sepetang, Perak, Malaysia, were utilized as raw materials. DSF, SPC, and SPI in the powder form were procured from Shandong Wonderful Biotech Co., Ltd. (Qingdao, China). Epichlorohydrin (ECH), NaOH, diethylenetriamine (DETA), and methylenesuccinic acid (IA) were supplied by Sigma-Aldrich Co., Ltd. (USA).

Presynthesized IA-PAE resin from our previous study with specific characteristics (solid content of 55.96 ± 0.01 wt%, pH of 6.68 at 27.58 °C, and apparent viscosity of 100.40 ± 0.25 mPa s) was employed [8]. The DSF-, SPC-, and SPI-based bio-adhesives were prepared at room temperature by suspending DSF (30 g), SPC (30 g), and SPI (12 g) in distilled water and were completely

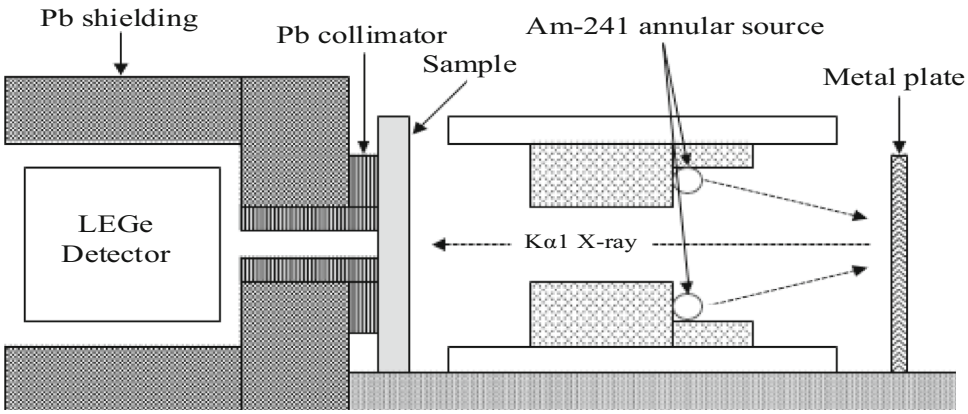

Fig. 1 Experimental setup

Table 1 Densities (ρ, gcm^{-3}) and elemental atomic compositions (weight fraction, %) of the investigated uncured and cured DSF-, SPC-, and SPI/NaOH/IA-PAE/*Rh.* spp. particleboards

Sample code	ρ	Weight faction of elements in each sample (%)													
		H	C	O	N	Na	Mg	P	S	Cl	K	Ca	Mn	Fe	Zn
DSF0	1.04	–	53.90	43.50	–	0.54	–	–	0.26	0.51	0.49	0.80	–	–	–
SPC0	1.11	–	53.74	44.18	–	0.46	–	–	0.05	0.34	–	0.50	–	0.73	–
SPI0	1.05	–	51.20	44.34	4.30	0.06	–	–	0.07	0.03	–	–	–	–	–
DSF1	1.08	–	53.77	43.43	2.15	0.06	0.04	–	–	0.24	0.17	0.14	–	–	–
SPC1	1.03	–	49.33	44.21	5.32	0.24	–	–	–	0.42	0.16	0.32	–	–	–
SPI1	1.07	–	48.21	44.08	7.13	–	0.13	–	–	0.19	–	0.25	–	–	–
DSF5	1.07	–	51.77	42.25	5.09	0.24	0.05	–	0.04	0.21	0.15	0.13	–	0.07	–
SPC5	1.09	–	51.24	43.04	4.43	0.17	–	0.11	0.10	0.48	0.23	0.20	–	–	–
SPI5	1.06	–	53.35	42.52	3.11	0.18	–	0.25	0.04	0.18	0.22	0.15	–	–	–
DSF10	1.09	–	49.62	45.09	4.22	0.18	0.13	–	–	0.41	0.14	0.21	–	–	–
SPC10	1.06	–	47.15	44.57	7.18	0.23	–	–	–	0.33	0.30	0.24	–	–	–
SPI10	1.08	–	48.27	44.30	5.95	0.20	–	–	–	0.38	0.47	0.43	–	–	–
DSF15	1.01	–	47.74	45.26	5.74	0.16	–	–	–	0.53	0.15	0.25	–	0.17	–
SPC15	1.01	–	46.07	45.26	7.24	0.32	–	–	–	0.37	0.23	0.17		0.34	–
SPI15	1.01	–	52.42	45.67	–	0.35	0.15	–	–	0.39	0.24	0.40	–	0.38	–
DSF5′	1.09	–	50.70	45.92	2.94	0.10	–	–	–	0.13	–	0.14	–	0.07	–
SPC5′	1.04	–	48.89	44.52	5.13	0.40	–	–	–	0.63	0.27	0.12	–	0.04	–
SPI5′	1.03	–	50.51	43.33	5.53	0.13	0.04	–	0.03	0.15	0.05	0.13	–	0.09	–
DSF10′	1.02	–	52.95	43.88	–	0.64	0.23	0.43	–	0.34	0.49	0.55	–	0.36	0.03
SPC10′	1.03	–	53.26	42.15	2.49	0.36	–	0.12	0.20	0.49	0.24	0.20	–	0.39	–
SPI10′	1.02	–	50.56	43.53	3.91	0.47	–	0.09	0.02	0.40	0.16	0.63	–	0.23	–
DSF15′	1.12	–	54.39	43.64	1.07	0.09	0.04	0.12	0.05	0.02	0.18	0.14	0.01	0.47	0.09
SPC15′	1.12	–	53.91	45.20	–	0.20	0.10	0.08	0.03	0.05	0.08	0.05	0.04	0.51	0.05
SPI15′	1.11	–	54.69	44.08	–	0.22	0.03	0.06	0.07	0.21	0.05	0.20	0.05	0.46	0.07

DSF0/SPC0/SPI0 = Binderless *Rh.* spp.; DSF1 = DSF/*Rh.* spp.; SPC1 = SPC/*Rh.* spp.; SPI1 = SPI/*Rh.* spp.; DSF5 = DSF/IA-PAE/*Rh.* spp.; SPC5 = SPC/IA-PAE/*Rh.* spp.; SPI5 = SPI/IA-PAE/*Rh.* spp.; DSF10 = DSF/IA-PAE/*Rh.* spp.; SPC10 = SPC/IA-PAE/*Rh.* spp.; SPI10 = SPI/IA-PAE/*Rh.* spp.; DSF15 = DSF/IA-PAE/*Rh.* spp.; SPC15 = SPC/IA-PAE/*Rh.* spp.; SPI15 = SPI/IA-PAE/*Rh.* spp.; DSF5′ = DSF/NaOH/IA-PAE/*Rh.* spp.; SPC5′ = SPC/NaOH/IA-PAE/*Rh.* spp.; SPI5′ = SPI/NaOH/IA-PAE/*Rh.* spp.; DSF10′ = DSF/NaOH/IA-PAE/*Rh.* spp.; SPC10′ = SPC/NaOH/IA-PAE/*Rh.* spp.; SPI10′ = SPI/NaOH/IA-PAE/*Rh.* spp.; DSF15′ = DSF/NaOH/IA-PAE/*Rh.* spp.; SPC15′ = SPC/NaOH/IA-PAE/*Rh.* spp.; and SPI15′ = SPI/NaOH/IA-PAE/*Rh.* spp. refer to 0, 5, 10, and 15 wt% IA-PAE, respectively.

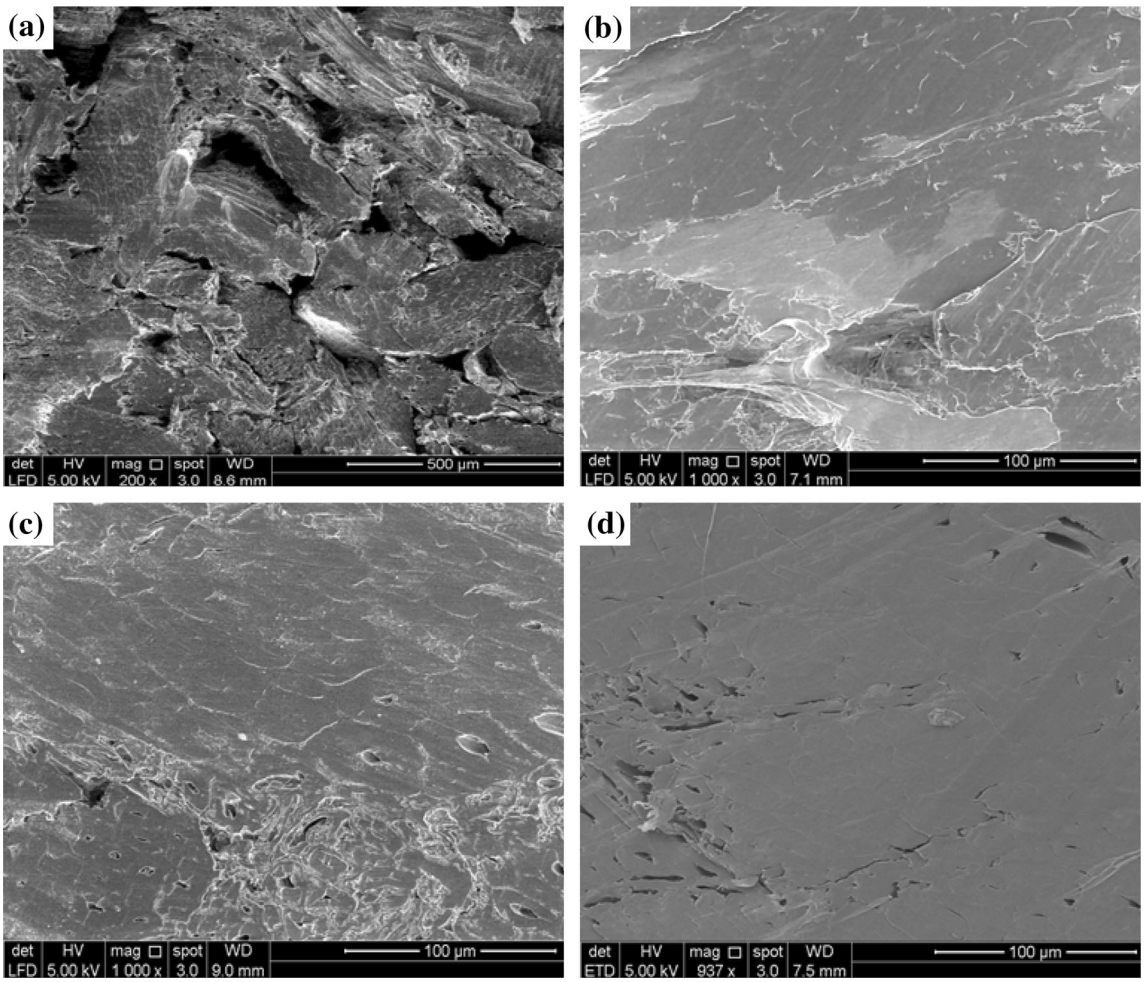

Fig. 2 SEM micrograph images of the uncured and cured particleboard composites: **a** DSF0/SPC0/SPI0, **b** DSF15′, **c** SPC15′, and **d** SPI15′

stirred at 600 rpm for 0.5 h to ensure good uniformity. The synthesized IA-PAE (0, 5, 10, and 15 wt%) was then added carefully to the slurry containing the adhesive mixtures and mixed for 0.5 h, to build up a series of DSF-, SPC-, and SPI-based adhesives. The resultant DSF-, SPC-, and SPI/IA-PAE mixtures were then alkalized with 2 N NaOH (10 wt%) solution to a pH of 11.0, mixed carefully for another 0.5 h to expedite dissolution and hydrolysis, ensuring high bonding strength in the resultant particleboards. The reaction temperature and time depended on the molar ratio of the resins. This indicates that the IA-PAE molecular weight strongly affected the subsequent bonding strength performance of particleboards.

Different combinations based on the DSF-, SPC-, and SPI/NaOH/IA-PAE concentrations were then thoroughly mixed with *Rh.* spp. wood (particle size, $\leq$ 74 µm) for 10 min, using a rotary mixer machine at 25,000 rpm to maintain homogeneity and remove voids. Using a preheated stainless steel mold with dimensions 30 × 30 × 1.0 cm^3, the mixtures were subsequently cold-compressed using a hydraulic press machine (0.49 MPa, 5 min, and 0 °C). The compressed samples were easily moved onto a hydraulic hot press machine (20 MPa, 20 min, and 180 °C) and manufactured as particleboards. This was followed by seven days of cooling and storage in an ambient environment, to avoid thermal stress and strain created by heat treatment and degradation of the resin. The pressing process consolidated the particle mats to the required density and thickness and polymerized the individual particle resin systems. The uncured and cured DSF-, SPC-, and SPI/NaOH/IA-PAE/*Rh.* spp. particleboard samples were assigned the following codes: DSF0, SPC0, SPI0, DSF1, SPC1, SPI1, DSF5, SPC5, SPI5, DSF10, SPC10, SPI10, DSF15, SPC15, SPI15, DSF5′, SPC5′, SPI5′, DSF10′, SPC10′, SPI10′, DSF15′, SPC15′, and SPI15′ for 0, 5, 10, and 15 wt%, respectively. The gravimetric approach was used for computing the average mass density of the particleboard samples.

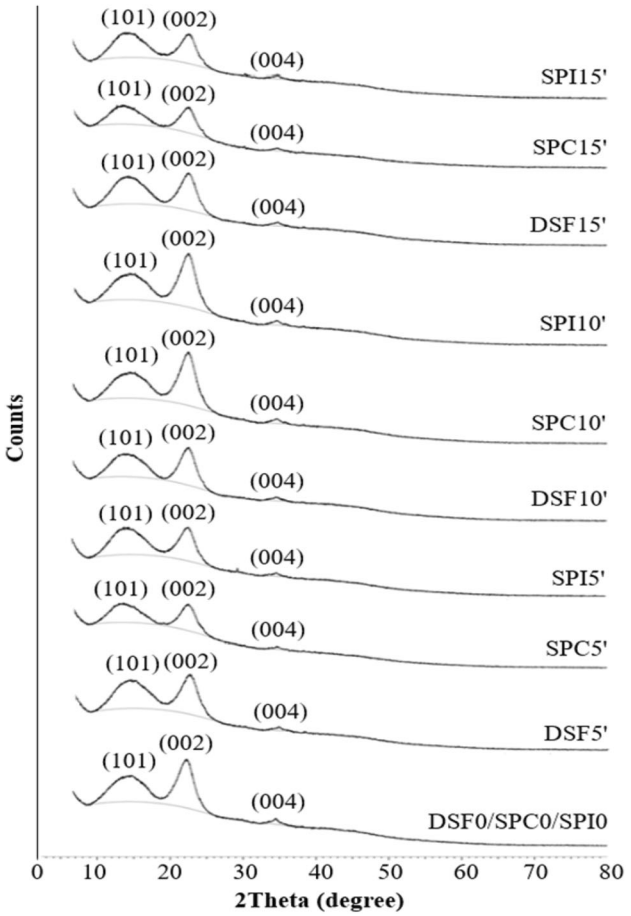

Fig. 3 XRD patterns for the DSF-, SPC-, and SPI/NaOH/IA-PAE/*Rh.* spp. particleboards, for various IA-PAE concentrations

2.2 Characterization of composites and theoretical calculations

2.2.1 Field emission scanning electron microscopy (FESEM) characterization

The morphological characteristics of DSF-, SPC-, and SPI/NaOH/IA-PAE/*Rh.* spp. particleboards were examined using an ultrahigh-resolution field emission scanning electron microscope (UHR-FESEM) (model FEI Quanta FEG-650, Netherlands). The samples were 60% gold-coated on the surfaces for 30 s at 45 mA, using a sputtering equipment to prevent charge build-up. The scanning electron microscopy (SEM) images of the particleboard crystallites were acquired at the magnification of up to 1000 ×, using an accelerating voltage in the 5–20 kV range, at a tilt angle of 30°.

2.2.2 X-ray diffraction (XRD) characterization

A Bruker D8 Advance XRD system was used for examining the crystalline structure of the particleboard samples. The samples were hydraulically pressed onto a sample holder into a circular disk (diameter, 2.5 cm). The XRD analysis pattern was run in a 2 θ scan, with the angle in the 5°–80° range, with Cu-$K_{\alpha 1}$ (λ = 0.15406 nm) as a target at 40 kV_P and 40 mA, at a scanning rate of 2°/min. All of the particleboard samples' data were analyzed using EVA 5 + software.

2.2.3 Mass attenuation and molar extinction coefficients

The mass attenuation coefficient (μ_m, cm^2/g) quantifies the probability of the photon interaction with a particleboard sample. It is an essential parameter for deriving other photon interaction related quantities, such as ε, $\sigma_{t,m}$, $\sigma_{t,a}$, $\sigma_{t,el}$, $X_{1/2}$, $X_{1/10}$, λ, Z_{eff}, and N_{el}. The measurements were performed using an X-ray attenuation setup fitted with a low-energy germanium (LEGe) detector system and other associated equipment, such as a multichannel analyzer (MCA-3 series), spectroscopy amplifier, high-voltage supply, a particleboard sample as the absorber, a radioactive source, a Pb shield, and a Pb collimator. The full width half maximum (FWHM) of the detector was 0.4 keV for 59.54 keV photons from an Am-241 source with the strength 3.7 × 10^9 Bq. The active crystal area and the diameter of the detector were 2 cm^2 and 1.6 cm, respectively, and the detector was kept at the liquid nitrogen temperature (–196 °C) during the experiments. X-ray fluorescence (XRF) photons from four metal plates (niobium, molybdenum, palladium, and stannum) were used for obtaining $K_{\alpha 1}$ photons with energies ranging from 16.59 keV to 25.26 keV. The distances between the particleboard samples–metal target plates and particleboard samples–detector were fixed at 7 cm and 8.9 cm, respectively, and the diameter of the Pb collimator was 0.3 cm. To reach statistical accuracy, each particleboard sample was assessed by collecting the spectra for a period of 0.6 × 10^3 s with observed dead time for all channels ranging from 31.82% to 34.07%. In addition, to eliminate the background and scattered photons, all of the measurements were performed inside a heavily shielded setup. The experimental measurements were repeated three times to determine the values of the selected parameters. The experimental setup is shown schematically in Fig. 1. Data collection and evaluation were performed using MAESTRO (an MCA emulation software program by ORTEC).

According to the well-known Beer-Lambert law, a parallel beam of monoenergetic X- and γ-ray photons is attenuated in matter according to the following exponential attenuation relation [8, 16]:

Table 2 Mass attenuation coefficients (μ_m), for uncured and cured DSF-, SPC-, and SPI-based *Rh.* spp. particleboards, for different photon energies

Sample code	16.59 keV		17.46 keV		21.21 keV		25.26 keV	
	μ_m (cm^2/g)	$\Delta\mu_m$ ± (%)	μ_m (cm^2/g)	$\Delta\mu_m$ ± (%)	μ_m (cm^2/g)	$\Delta\mu_m$ ± (%)	μ_m (cm^2/g)	$\Delta\mu_m$ ± (%)
DSF0	1.096	0.018	0.914	0.015	0.620	0.031	0.435	0.023
SPC0	1.088	0.015	0.921	0.047	0.611	0.035	0.438	0.029
SPI0	1.102	0.026	0.919	0.016	0.622	0.024	0.440	0.017
DSF1	1.049	0.037	0.925	0.030	0.638	0.025	0.429	0.011
SPC1	1.033	0.019	0.916	0.011	0.559	0.030	0.414	0.041
SPI1	1.057	0.023	0.949	0.015	0.633	0.018	0.428	0.010
DSF5	1.095	0.016	0.988	0.047	0.652	0.019	0.451	0.023
SPC5	1.087	0.035	0.965	0.013	0.611	0.022	0.426	0.037
SPI5	1.098	0.011	0.979	0.031	0.583	0.024	0.449	0.015
DSF10	1.069	0.035	0.998	0.012	0.670	0.022	0.465	0.016
SPC10	1.071	0.026	0.985	0.033	0.654	0.035	0.418	0.041
SPI10	1.091	0.018	0.992	0.022	0.655	0.017	0.437	0.015
DSF15	1.084	0.021	0.997	0.043	0.660	0.014	0.460	0.016
SPC15	1.076	0.016	0.969	0.012	0.651	0.027	0.452	0.018
SPI15	1.089	0.031	0.944	0.014	0.593	0.025	0.458	0.011
DSF5′	1.044	0.025	0.957	0.037	0.645	0.023	0.442	0.018
SPC5′	1.027	0.012	0.965	0.016	0.599	0.017	0.434	0.013
SPI5′	1.081	0.022	0.943	0.035	0.603	0.026	0.446	0.020
DSF10′	1.060	0.031	0.961	0.050	0.653	0.012	0.465	0.016
SPC10′	1.066	0.012	0.972	0.023	0.629	0.022	0.454	0.014
SPI10′	1.097	0.028	0.964	0.023	0.616	0.018	0.461	0.020
DSF15′	1.105	0.030	1.010	0.016	0.747	0.022	0.499	0.017
SPC15′	1.095	0.012	1.023	0.019	0.686	0.022	0.485	0.011
SPI15′	1.102	0.012	1.031	0.012	0.740	0.017	0.494	0.014

$$\mu_m = \frac{\mu}{\rho} = \frac{1}{\rho x}\ln\left(\frac{I_o}{I_t}\right), \tag{1}$$

where I_o and I_t indicate the incident intensity and transmitted intensity of the photons, respectively, while ρ and x denote the density and physical thickness of the particleboard samples. In the case of a multi-element material (i.e., a chemical compound or a homogeneous mixture) constituting the sample, μ_m can be obtained from the weighted sum of the contributions of individual atoms as in Eq. (2) [17]:

$$(\mu_m)_{DSF-SPC-SPIcomposite} = \sum_{j=1}^{r}\left\{\left(\frac{n_j A_j}{\sum_j n_j A_j}\right).\left(\frac{\mu}{\rho}\right)_j\right\}, \tag{2}$$

where n_j, A_j, ρ, $\sum_j n_j A_j$, and $\left(\frac{\mu}{\rho}\right)_j$ denote the number of atoms, effective atomic weight, density, molecular weight, and mass attenuation coefficient of the jth constituent element ($j = 1, 2, 3, \ldots, r$), for a particular photon energy being considered. The overall mass attenuation coefficient ($\mu_{m(total)}$, cm^2/g) is the sum of the attenuation coefficients for photoelectric absorption, Compton scattering, and pair production for a given photon energy, and it is given as:

$$\mu_{m(total)} = \mu_{Photoelectric} + \mu_{Compton} + \mu_{pair-production}. \tag{3}$$

On the other hand, the molar extinction coefficient (ε, cm^2/mol) is the attenuation produced by one mole of the substance and can be obtained as follows:

$$\varepsilon = \log_{10} e\left(\mu_m \sum_j n_j A_j\right) = 0.434\mu_m \sum_j n_j A_j. \tag{4}$$

2.2.4 *Effective atomic number and effective electron density*

In medical radiation dosimetry, the effective atomic number (Z_{eff}, dimensionless quantity) and effective electron density (N_{el}, electron/g) are remarkable parameters used for ascertaining the radiation absorption in human tissues and dosimetric phantoms. The value of Z_{eff} informs about the material subjected to radiation, and the Z_{eff} values of complex materials are used in the computations of absorbed dose for radiation therapy [18]. The Z_{eff} value for

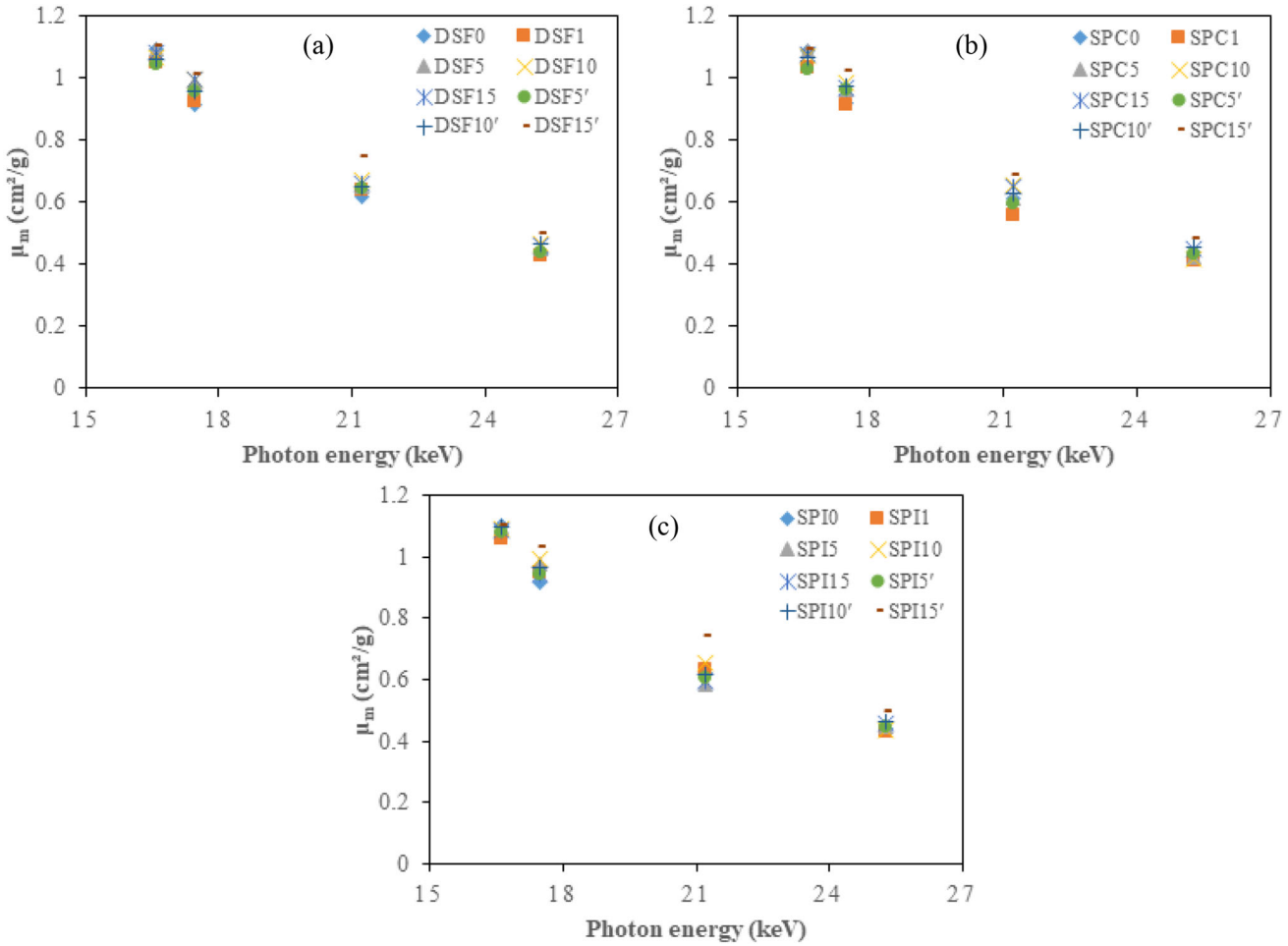

Fig. 4 (Color online) Mass attenuation coefficients for DSF-, SPC-, and SPI/NaOH/IA-PAE/*Rh.* spp. particleboards: **a** DSF-based, **b** SPC-based, and **c** SPI-based

the presently studied composite particleboard samples was computed from the respective atomic compositions, as follows:

$$Z_{\text{eff}} = \frac{\frac{1}{N_{\text{A}}}\sum_{j=1}^{r}\left\{f_j A_j \left(\frac{\mu}{\rho}\right)_j\right\}}{\frac{1}{N_{\text{A}}}\sum_{j=1}^{r}\left\{\frac{f_j A_j}{Z_j}\left(\frac{\mu}{\rho}\right)_j\right\}} = \frac{\sum_{j=1}^{r}\left\{f_j A_j \left(\frac{\mu}{\rho}\right)_j\right\}}{\sum_{j=1}^{r}\left\{\frac{f_j A_j}{Z_j}\left(\frac{\mu}{\rho}\right)_j\right\}}, \tag{5}$$

where $f_j = \frac{n_j}{\sum_j n_j}$ is the fractional abundance of element j relative to the number of atoms, subject to $\sum_j^r f_j = 1$, N_{A} is Avogadro's constant, and Z_j is the atomic number. The value of Z_{eff} can also be assessed from the percentage elemental compositions of the sample specimens using ultrahigh-resolution field emission scanning electron microscope-energy dispersive X-ray (UHR-FESEM-EDX) spectrometry, and it is given by Eq. (6) [8, 19]:

$$Z_{\text{eff}} = \left[\sum_{j=1}^{N}\frac{N_g^j}{N_g} z_j^{3.4}\right]^{1/3.4} = \left[\sum_{j=1}^{N}\frac{\omega_j z_j / A_j}{\sum_j\left(\omega_j z_j / A_j\right)} z_j^{3.4}\right]^{1/3.4}, \tag{6}$$

where N_g^j and ω_j are the number of electrons per unit volume of the mixture and weight ratio of the j^{th} constituent element. The elemental compositions, along with Z_{eff} and respective density values of the investigated uncured and cured DSF-, SPC-, and SPI-based *Rh.* spp. particleboards are listed in Table 1. N_{el} is closely related to Z_{eff} by Eq. (7) [20]:

$$N_{\text{el}} = \frac{N_{\text{A}}}{\sum_J n_j A_j} Z_{\text{eff}} \sum_J n_j = N_{\text{A}} \frac{Z_{\text{eff}}}{A}, \tag{7}$$

$$A = \frac{\sum_J n_j A_j}{\sum_J n_j}, \tag{8}$$

$$Z = \frac{n_i Z_i}{n}, \tag{9}$$

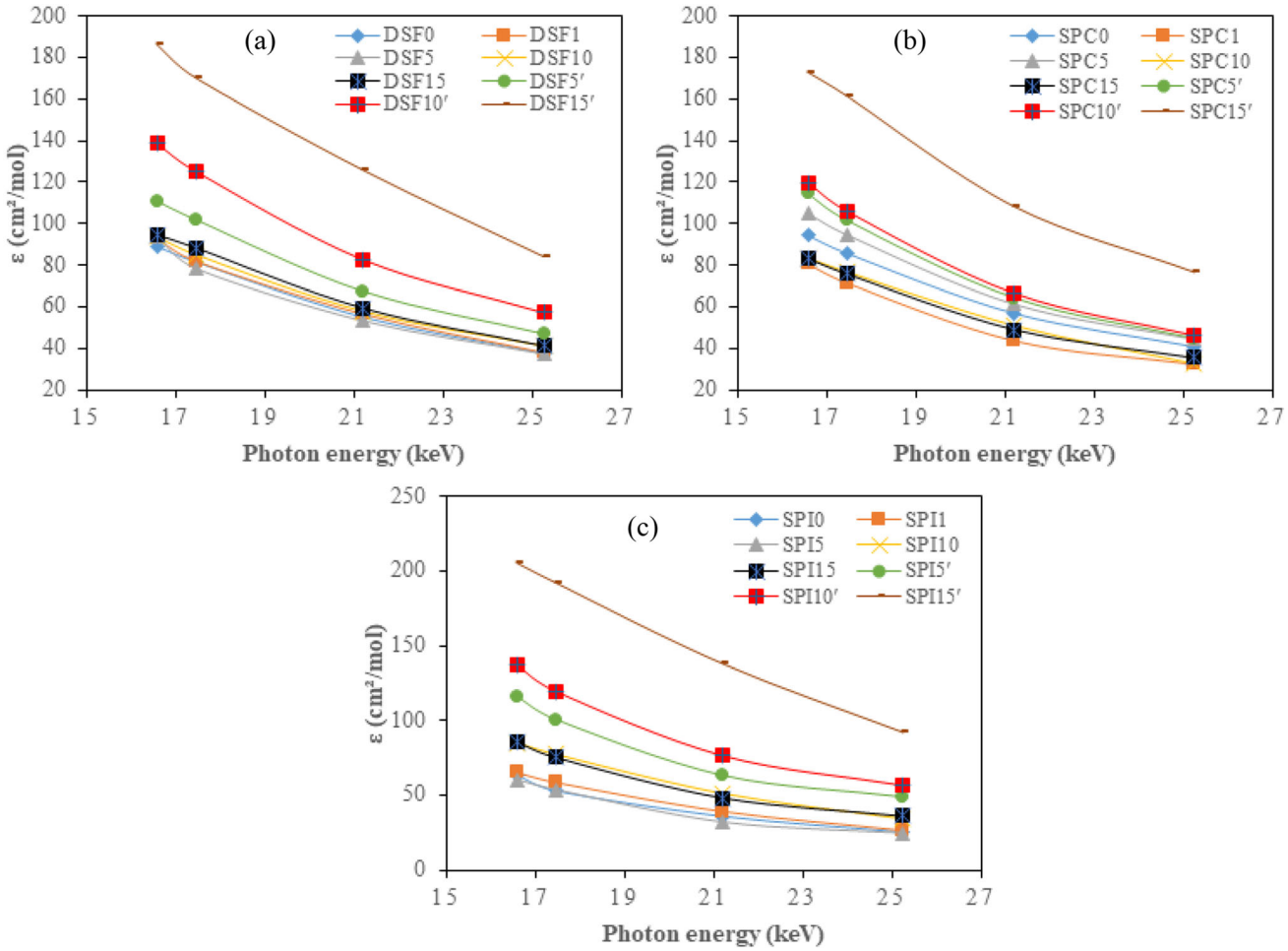

Fig. 5 (Color online) Dependence of the molar extinction coefficients on the photon energy, for the DSF-, SPC-, and SPI/NaOH/IA-PAE/*Rh.* spp. particleboards: **a** DSF-based, **b** SPC-based, and **c** SPI-based

where A and Z denote, respectively, the mean atomic weight and atomic number of the composite material.

2.2.5 HVL, TVL, and MFP

HVL ($X_{1/2}$, cm) is one of the most appropriate parameters for estimating the effective attenuating ability of a particleboard material with respect to photons. It can be expressed as the thickness of the material needed for reducing the radiation intensity by 50%, and it is given by [8, 21]:

$$X_{1/2} = \frac{0.693}{\mu}. \tag{10}$$

Similarly, TVL ($X_{1/10}$, cm) corresponds to the thickness of the absorber required for attenuating the radiation intensity by 90%, and it is given by:

$$X_{1/10} = \frac{2.303}{\mu}. \tag{11}$$

Likewise, MFP (λ, cm), which plays a critical role in understanding the exponential attenuation of photons, is the mean distance traveled by a photon before it interacts, and it is given by Eq. (12):

$$\lambda = \frac{1}{\mu}. \tag{12}$$

These are the most widely used raw parameters for composite materials that characterize the efficiency of radiation shielding. Particleboard sample materials for incident photons with the lowest values of $X_{1/2}$, $X_{1/10}$, and λ demonstrate good radiation shielding properties and are better suitable for shielding against ionizing radiation for radiation protection applications [22].

2.2.6 Total molecular, effective atomic, and electronic cross sections

The expressions for the total molecular ($\sigma_{t,m}$, cm^2/-molecule), effective atomic ($\sigma_{t,a}$, cm^2/atom), and electronic

Table 3 Effective atomic numbers (Z_{eff}) for the uncured and cured DSF-, SPC-, and SPI-based *Rh.* spp. particleboards, for different photon energies

Sample code	16.59 keV	17.46 keV	21.21 keV	25.26 keV
DSF0	12.538 ± 0.100	10.945 ± 0.118	10.131 ± 0.064	9.010 ± 0.120
SPC0	12.655 ± 0.168	11.048 ± 0.122	10.177 ± 0.126	9.038 ± 0.133
SPI0	11.906 ± 0.121	11.261 ± 0.130	10.153 ± 0.111	9.026 ± 0.091
DSF1	10.830 ± 0.167	10.339 ± 0.127	10.448 ± 0.152	9.404 ± 0.126
SPC1	10.615 ± 0.104	10.316 ± 0.158	10.363 ± 0.144	9.311 ± 0.077
SPI1	10.811 ± 0.130	11.001 ± 0.109	10.401 ± 0.132	9.518 ± 0.105
DSF5	11.705 ± 0.095	10.782 ± 0.115	10.777 ± 0.146	9.784 ± 0.169
SPC5	11.958 ± 0.173	10.526 ± 0.121	10.635 ± 0.141	9.752 ± 0.132
SPI5	11.853 ± 0.111	10.631 ± 0.146	10.668 ± 0.172	9.687 ± 0.145
DSF10	12.461 ± 0.150	11.834 ± 0.129	10.809 ± 0.119	9.944 ± 0.101
SPC10	12.204 ± 0.108	11.757 ± 0.131	10.957 ± 0.103	9.983 ± 0.141
SPI10	12.533 ± 0.161	11.614 ± 0.150	10.981 ± 0.180	9.907 ± 0.111
DSF15	13.469 ± 0.185	12.015 ± 0.136	11.101 ± 0.117	10.216 ± 0.127
SPC15	14.072 ± 0.143	11.978 ± 0.105	11.079 ± 0.136	10.308 ± 0.123
SPI15	13.476 ± 0.102	11.947 ± 0.185	11.062 ± 0.140	10.279 ± 0.057
DSF5′	14.704 ± 0.136	12.348 ± 0.107	11.388 ± 0.151	10.493 ± 0.160
SPC5′	14.669 ± 0.128	12.242 ± 0.161	11.294 ± 0.129	10.450 ± 0.144
SPI5′	14.594 ± 0.140	12.336 ± 0.172	11.356 ± 0.135	10.515 ± 0.101
DSF10′	15.163 ± 0.116	12.690 ± 0.133	11.616 ± 0.064	10.688 ± 0.173
SPC10′	15.195 ± 0.102	12.840 ± 0.175	11.745 ± 0.103	10.723 ± 0.159
SPI10′	14.964 ± 0.162	12.731 ± 0.181	11.628 ± 0.155	10.620 ± 0.142
DSF15′	15.942 ± 0.185	13.115 ± 0.120	11.979 ± 0.161	10.974 ± 0.138
SPC15′	16.033 ± 0.104	13.106 ± 0.154	12.128 ± 0.159	10.928 ± 0.145
SPI15′	15.839 ± 0.127	13.110 ± 0.097	11.977 ± 0.133	10.961 ± 0.111

($\sigma_{t,el}$, cm^2/electron) cross sections are given in the following equations [23]:

$$\sigma_{t,m} = \frac{1}{N_A}(\mu_m)_{DSF-SPC-SPIcomposite}\sum_j n_j A_j, \tag{13}$$

$$\sigma_{t,a} = \frac{1}{N_A}\sum_j f_j A_j \left(\frac{\mu}{\rho}\right)_j = \frac{(\mu_m)_{DSF-SPC-SPIcomposite}}{N_A \sum_j \left(\frac{\omega_j}{A_j}\right)} = \frac{\sigma_{t,m}}{\sum_j n_j}, \tag{14}$$

$$\sigma_{t,el} = \frac{1}{N_A}\sum_j \left(\frac{f_j A_j}{Z_j}\right)\left(\frac{\mu}{\rho}\right)_j = \frac{\sigma_{t,a}}{Z_{eff}} = \frac{\mu_m}{N_{el}}. \tag{15}$$

The experimental error associated with the measurement of μ_m was estimated using the following relation:

$$(\Delta\mu_m)^2 = \left(\frac{1}{\rho_t}\right)^2\left[\left(\frac{\Delta I_t}{I_t}\right)^2 + \left(\frac{\Delta I_o}{I_o}\right)^2 + \left(\ln\frac{\Delta I_o}{I_t}\right)^2 \cdot \left(\frac{\Delta\rho_t}{\rho_t}\right)^2\right], \tag{16}$$

where $\Delta I_t, \Delta I_o$ and $\Delta\rho_t$ correspond to the uncertainties (estimated errors) in the intensities I_t, I_o and areal density of the composite sample material, respectively.

3 Results and discussion

3.1 Analysis of SEM images

The micrograph images of the uncured and cured particleboard composites are shown in Fig. 2a–d. Figure 2a reveals an agglomeration of fibers, an irregular fracture surface, and micro-cracks that exist in the uncured particleboard composites despite the compression forced onto the cell walls and parenchyma tissue during the hot pressing. The observed void spaces and gaps by the lumen can be attributed to the non-homogeneous distribution of particle sizes, which could decrease the compactness and weaken the bonding between the fiber and the matrix, thus affecting the ability of samples DSF0, SPC0, and SPI0 to serve as X-ray radiation shielding materials. However, Fig. 2b–d, with more uniform distribution of particles owing to their weaker agglomeration and better particle dispersion, show a well-formed crystal of the cured particleboard composites. As a result, no isolate nanoparticles are observed, implying that with increasing attenuation of incident photons, DSF15′, SPC15′, and SPI15′ exhibit better X-ray attenuation ability. The oxidized IA-PAE and ring-opened azetidinium cross-linking can explain

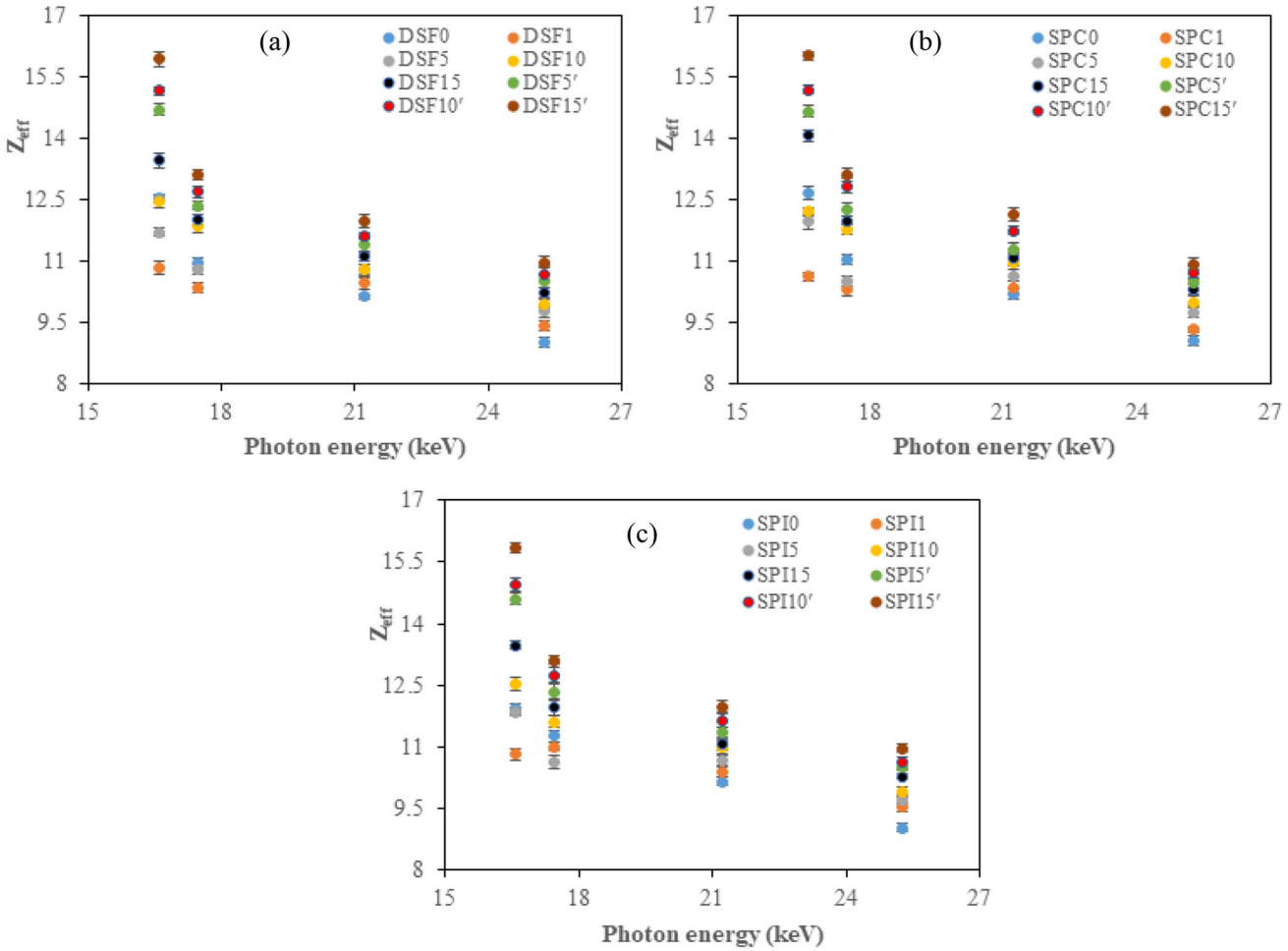

Fig. 6 (Color online) Effective atomic number versus the photon energy, for the DSF-, SPC-, and SPI/NaOH/IA-PAE/*Rh.* spp. particleboards: **a** DSF-based, **b** SPC-based, and **c** SPI-based samples

relatively smooth and compact fracture surfaces [8]. Thus, the morphologies of the DSF-, SPC-, and SPI-based particleboard composites are markedly affected by the concentration of NaOH/IA-PAE, thereby improving water resistance and advanced compact cross section formation. Thus, DSF15′, SPC15′, and SPI15′ particleboard composites exhibit uniform densities throughout the samples. Therefore, these composites are likely to exhibit better radiation shielding characteristics.

3.2 XRD analysis

All of the XRD patterns in Fig. 3 indicate preferential (101), (002), and (004) orientations, which are assigned predominant peaks at 2 θ in the 13.29°–14.67°, 22.20°–22.37°, and 34.52°–34.61° ranges for DSF-based particleboards, whereas for SPC-based particleboards, the predominant peaks appear in the 13.09°–14.70°, 22.12°–22.41°, and 34.48°–34.75° ranges, respectively. On the other hand, SPI-based samples exhibit predominant peaks approximately in the 13.68°–14.67°, 22.27°–22.39°, and 34.40°–34.72° ranges, respectively. All of the peaks exhibited by the particleboard samples are in excellent agreement with the reported data by the Joint Committee on Powder Diffraction Standards (JCPDS), card no. 36–1451 [24]. Figure 3 clearly shows that in all of the considered cases, the intensities of the (101) and (004) peaks are low, compared with the (002) reflection peak. This indicates that the preferential orientation of the crystallites in the (002) orientation is in the direction perpendicular to the substrate. Moreover, the observed crystallinity index values for the DSF-, SPC-, and SPI-based samples varied in the 36.67–41.58%, 27.98–42.90%, and 29.99–43.12% ranges, respectively, suggesting the predominance of an amorphous phase. Obviously, all of the studied samples had a typical FWHM in the 0.04°–2.23° range. The proportionate observed values of the crystallinity index indicate that denser structures were formed in the DSF-, SPC-, and SPI/NaOH/IA-PAE/*Rh.* spp. samples, improving the water resistance, consistent with the

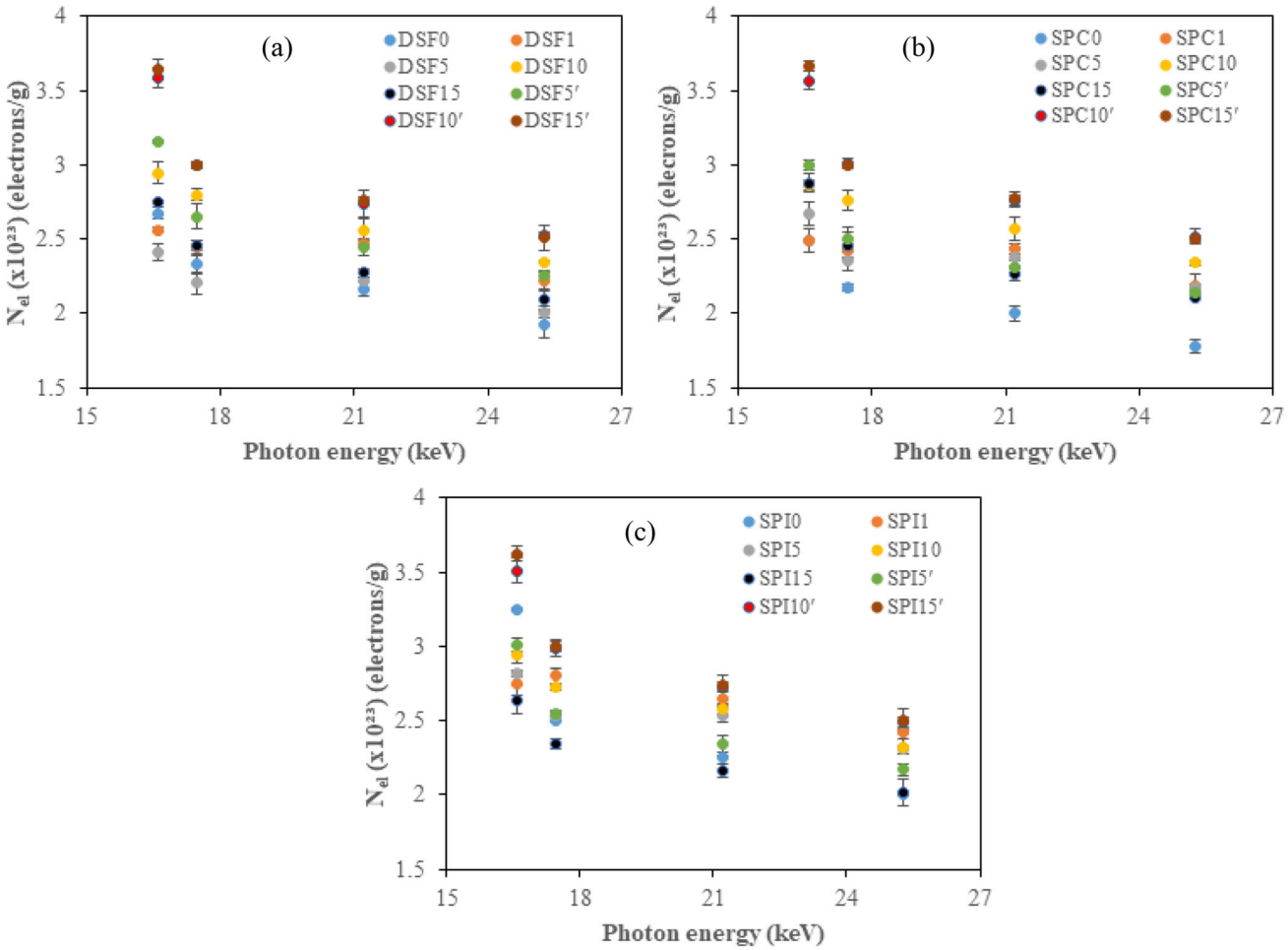

Fig. 7 (Color online) Effective electron density of the DSF-, SPC-, SPI/NaOH/IA-PAE/*Rh.* spp. particleboards, versus the incident photon energy: **a** DSF-based, **b** SPC-based, and **c** SPI-based samples

SEM analysis. This can be ascribed to the cross-linked and interpenetrating structure created by NaOH/IA-PAE with *Rh.* spp. These results support the suitability of DSF-, SPC-, and SPI/NaOH/IA-PAE-based *Rh.* spp. particleboards as convenient radiological safety materials for medical applications.

3.3 Elemental atomic compositions, mass attenuation coefficients, and molar extinction coefficients of DSF-, SPC-, and SPI/NaOH/IA-PAE/*Rh.* spp. particleboards

The elemental compositions of the presently studied uncured and cured DSF-, SPC-, and SPI/NaOH/IA-PAE-based *Rh.* spp. particleboard samples are listed in Table 1. Both the atomic numbers and atomic weights of the elements found in the particleboard samples were taken from a recent IUPAC technical report [25]. The shielding properties of the DSF-, SPC-, and SPI-based samples increased proportionally with increasing the Fe content from the IA-PAE, which is likely to be advantageous for using these materials in shielding. The μ_m values were computed at the specific energies for the three soy protein-based *Rh.* spp. particleboard samples, as shown in Table 2, and the results are shown in Fig. 4a–c. These findings are consistent with the results obtained for different composite materials, such as silicate, borate heavy metal oxide glasses, geological materials, and biological matters [1, 3, 5, 26]. It is evident from Table 1 that all of the presently considered samples have appropriate densities ranging from 1.01 to 1.12 g/cm^3, with optimal values for DSF15′, SPC15′, SPI15′, and SPC0 particleboards. In contrast to lower-density absorbing materials, several primary X-ray beams were attenuated by DSF15′, SPC15′, SPI15′, and SPC0. Owing to closely packed particles, the possibility of X-ray interaction with the atoms of the absorbing material is relatively high [3]. It can be seen that the μ_m values of the particleboard samples are affected by the IA-PAE concentration, and for all of the IA-PAE addition levels, the μ_m values decrease exponentially with

Table 4 Effective electron density ($N_{el} \times 10^{23}$) (electrons/g) values for the uncured and cured DSF-, SPC-, and SPI-based *Rh.* spp. particleboards, for different photon energies

Sample code	16.59 keV	17.46 keV	21.21 keV	25.26 keV
DSF0	2.674 ± 0.042	2.334 ± 0.068	2.160 ± 0.043	1.921 ± 0.091
SPC0	2.488 ± 0.079	2.172 ± 0.020	2.001 ± 0.050	1.777 ± 0.046
SPI0	3.247 ± 0.006	2.504 ± 0.015	2.257 ± 0.009	2.007 ± 0.013
DSF1	2.559 ± 0.017	2.443 ± 0.049	2.468 ± 0.026	2.222 ± 0.058
SPC1	2.491 ± 0.013	2.421 ± 0.040	2.432 ± 0.035	2.185 ± 0.074
SPI1	2.754 ± 0.080	2.802 ± 0.055	2.649 ± 0.041	2.425 ± 0.016
DSF5	2.415 ± 0.056	2.205 ± 0.071	2.224 ± 0.015	2.010 ± 0.039
SPC5	2.671 ± 0.081	2.351 ± 0.060	2.375 ± 0.073	2.178 ± 0.021
SPI5	2.817 ± 0.022	2.530 ± 0.038	2.539 ± 0.054	2.305 ± 0.030
DSF10	2.944 ± 0.075	2.796 ± 0.040	2.554 ± 0.081	2.349 ± 0.010
SPC10	2.864 ± 0.038	2.759 ± 0.066	2.571 ± 0.080	2.343 ± 0.017
SPI10	2.941 ± 0.053	2.726 ± 0.017	2.577 ± 0.036	2.325 ± 0.049
DSF15	2.755 ± 0.011	2.458 ± 0.032	2.271 ± 0.024	2.091 ± 0.062
SPC15	2.879 ± 0.064	2.451 ± 0.090	2.267 ± 0.051	2.109 ± 0.016
SPI15	2.642 ± 0.097	2.342 ± 0.031	2.168 ± 0.045	2.015 ± 0.090
DSF5′	3.156 ± 0.014	2.651 ± 0.086	2.445 ± 0.060	2.253 ± 0.031
SPC5′	3.001 ± 0.033	2.505 ± 0.070	2.311 ± 0.039	2.138 ± 0.027
SPI5′	3.012 ± 0.048	2.546 ± 0.011	2.343 ± 0.052	2.169 ± 0.043
DSF10′	3.582 ± 0.069	2.998 ± 0.023	2.740 ± 0.091	2.525 ± 0.020
SPC10′	3.566 ± 0.060	3.013 ± 0.025	2.756 ± 0.037	2.516 ± 0.049
SPI10′	3.512 ± 0.084	2.988 ± 0.061	2.729 ± 0.080	2.492 ± 0.031
DSF15′	3.644 ± 0.071	2.997 ± 0.023	2.758 ± 0.025	2.508 ± 0.080
SPC15′	3.664 ± 0.029	2.995 ± 0.014	2.772 ± 0.047	2.498 ± 0.016
SPI15′	3.620 ± 0.051	2.996 ± 0.033	2.737 ± 0.029	2.505 ± 0.070

increasing photon energy [3, 8, 17]. However, this decrease is more apparent for high energies. In addition, photoelectric absorption is the dominant attenuation mechanism in the present study, which is more likely to interfere with photons as its cross section varies with the atomic number as Z^4 and Z^5 in low- and high-energy regions, respectively, and scales with energy as $E^{3.5}$ [3, 27]. It is apparent from Table 2 and Fig. 4a–c that the μ_m values for each of the DSF-, SPC-, and SPI-based particleboard samples decreased very sharply for the 1.105 ± 0.030–0.429 ± 0.011 (cm^2/g), 1.095 ± 0.012–0.414 ± 0.041 (cm^2/g), and 1.102 ± 0.012–0.429 ± 0.010 (cm^2/g) ranges, as the photon energy changed from 16.59–25.26 keV. Based on Fig. 4a–c, it is obvious that among the selected samples, the DSF15′, SPC15′, and SPI15′ samples had the highest values of μ_m, since they were the most densest. This is because the highest amounts of carbon, oxygen, and other elements were contained in these particleboard samples (Table 1). It is also possible to attribute the presence of higher carbon and oxygen concentrations to the high percentage of their flow at high temperatures in the composite samples. This can also be owing to the chemical composition of DSF, SPC, SPI, NaOH/IA-PAE, and *Rh.* spp. particles, and significantly affects DSF15′, SPC15′, and SPI15′ particleboards, which can help to improve their performance in radiation shielding applications. These findings suggest that, relative to the other sample composite formulations, 15 wt% IA-PAE better attenuates 16.59–25.26 keV photons, because these photons interact primarily through the photoelectric effect with the absorbing material. These results confirm the validity of DSF-, SPC-, and SPI/NaOH/*Rh.* spp. with 15 wt% IA-PAE as appropriate radiation shielding materials.

Figure 5a–c clearly show the dependence of molar extinction coefficients for DSF/NaOH/IA-PAE/*Rh.* spp., SPC/NaOH/IA-PAE/*Rh.* spp., and SPI/NaOH/IA-PAE/*Rh.* spp. particleboards on the incident photon energy. Clearly, ε for all of the studied particleboard samples depends inversely on the photon energy, and the trend is identical to that of μ_m. From these figures, ε values reached their maxima in the 88.976–186.164 (cm^2/mol) range for DSF-based particleboards, 94.250–172.861 (cm^2/mol) range for SPC-based particleboards, and 60.292–205.235 (cm^2/mol) range for SPI-based particleboards, at the selected photon energies; the photoelectric effect plays a dominant role. In addition, from Fig. 5a–c, ε increases with IA-PAE for all selected particleboard samples, but tends to decrease sharply with increasing photon energy, which could be

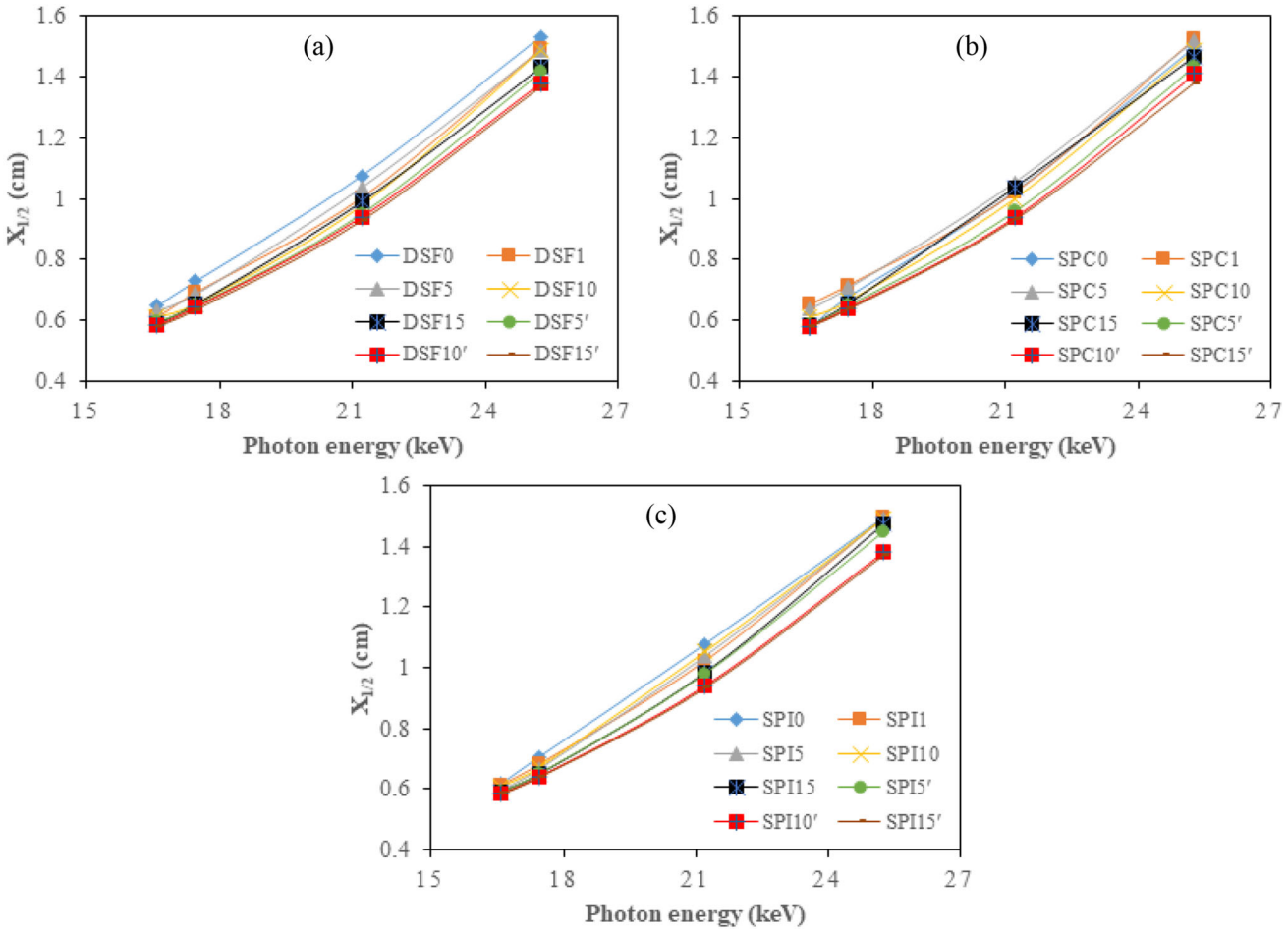

Fig. 8 (Color online) HVL values of the studied particleboard samples versus the photon energy: **a** DSF-based, **b** SPC-based, and **c** SPI-based

attributed to the high molecular weight of IA-PAE. The DSF15′, SPC15′, and SPI15′ samples exhibit the highest ε among the DSF-, SPC-, and SPI-based particleboard samples because of their higher number of atoms compared with the other samples, which means their molecular weight is higher, compared with the other samples. The higher values of ε for the DSF15′, SPC15′, and SPI15′ particleboards suggest better shielding properties, compared with the other particleboard samples.

3.4 Effective atomic numbers and effective electron densities of the DSF-, SPC-, and SPI/NaOH/IA-PAE/*Rh.* spp. particleboards

The evaluated values of Z_{eff} and experimental uncertainties for the current samples are listed in Table 3. Some typical plots of Z_{eff} versus the photon energy are shown in Fig. 6a–c. The behavior of Z_{eff} for all of the particleboards was almost identical. Similar trend was observed for different materials, such as biological compounds, concretes, alloys, and glass systems [28–31]. The value of Z_{eff} for the DSF-, SPC-, and SPI/NaOH/IA-PAE/*Rh.* spp. particleboards increased with increasing the IA-PAE modifier content and appeared to decrease with increasing incident photon energy, as in the case of μ_m and ε. This suggests that, at low energies, photons are more likely to interact with particleboards. As shown in Table 3, the Z_{eff} values for all of the studied particleboard samples are in the 9.010 ± 0.120–16.033 ± 0.104 range. In addition, the Z_{eff} values for all of the studied samples varied significantly with the atomic number of the constituent elements in the studied composite samples [31]. The atoms of higher–atomic–number absorbing material are more likely to encounter photon targets; thus, the interaction probability is relatively high owing to the photoelectric interaction. Therefore, the likelihood of X-ray attenuation occurring in the sample is high. Thus, the higher values of Z_{eff} observed at low photon energies are owing to the contribution of the photoelectric absorption, which is more likely, compared with the Compton scattering and pair production processes. Therefore, Z_{eff} for the total photon interaction is high at low photon energies and low at high photon energies, with

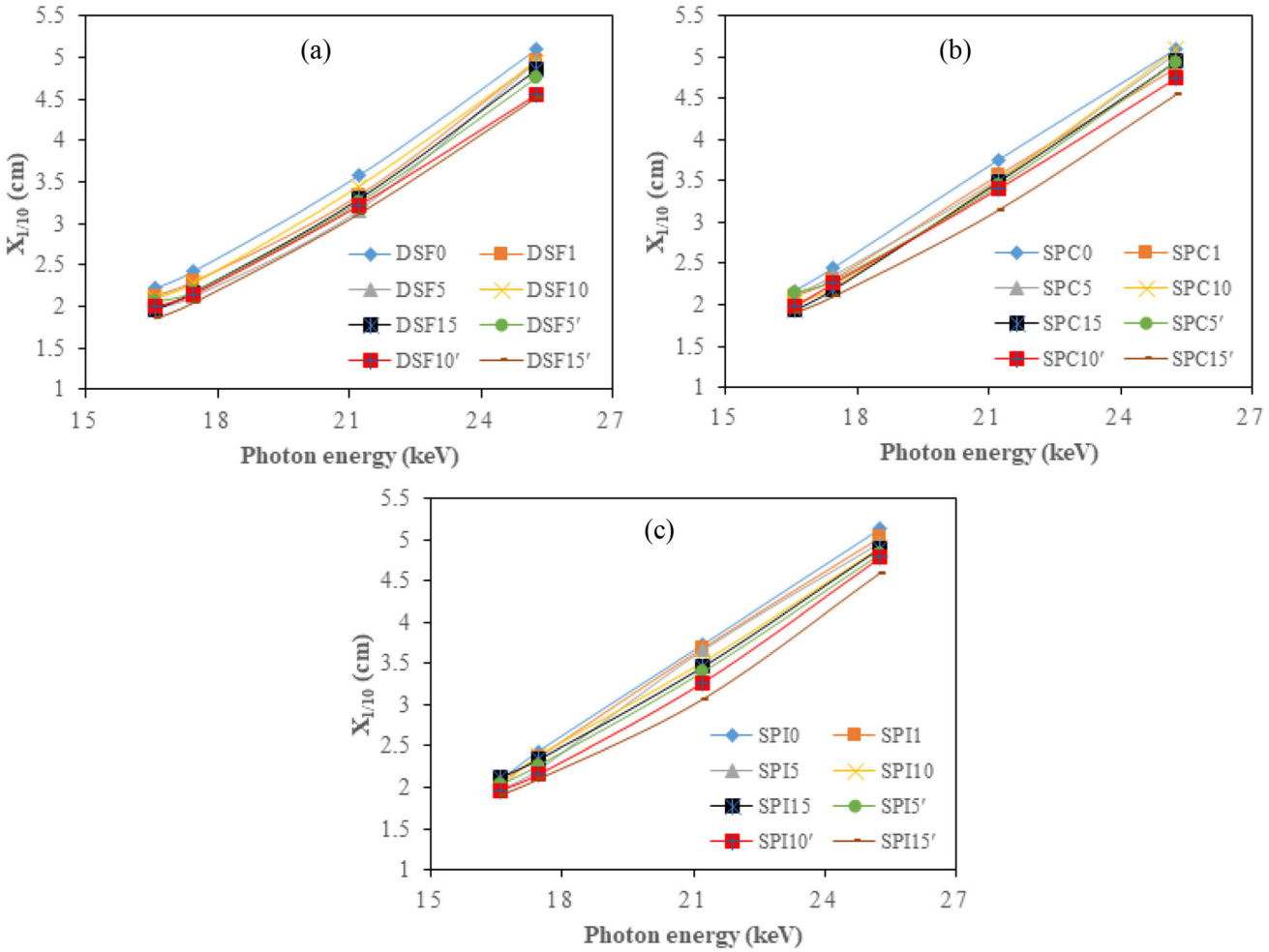

Fig. 9 (Color online) Dependence of the TVL values on the incident photon energy, for the studied particleboard samples: **a** DSF-based, **b** SPC-based, and **c** SPI-based

a peak owing to the photoelectric effect in the studied particleboard samples, which occurs around the K-absorption edge of the medium-Z element. It can be seen from Fig. 6a–c that the maximal values of Z_{eff} were observed for DSF15′, SPC15′, and SPI15′, respectively, which can be explained by the chemical composition and relatively high values of μ_m in these samples, compared with the other samples. This improvement in the Z_{eff} values of DSF15′, SPC15′, and SPI15′ with an enhancement in the IA-PAE concentration suggests that the shielding ability of the particleboards can be improved by incorporating NaOH/IA-PAE. The minimal Z_{eff} values were found to effectively correspond to DSF0, SPC0, and SPI0, respectively, at 25.26 keV. This can be explained by noting that as the photon energy increased, the Z_{eff} value could decrease owing to the increased transmission of incident photons through the particleboard material, reducing photon attenuation in the particleboard samples. Therefore, the DSF15′, SPC15′, and SPI15′ particleboard exhibited the highest photon shielding efficiency.

The estimated N_{el} values for the different particleboard samples are summarized in Table 4. In addition, the dependence of N_{el} on the incident photon energy is shown in Fig. 7a–c. Evidently, both the N_{el} and Z_{eff} values are closely related, and a similar trend was noticed for the dependence of N_{el} on the incident photon energy, since N_{el} is directly proportional to Z_{eff}, as is evident from Fig. 7a–c. The N_{el} values for the different photon energy ranges were $1.921 \pm 0.091 \times 10^{23}$–$3.644 \pm 0.071 \times 10^{23}$ (electrons/g), $1.777 \pm 0.046 \times 10^{23}$–$3.664 \pm 0.029 \times 10^{23}$ (electron/g), and $2.007 \pm 0.013 \times 10^{23}$–$3.620 \pm 0.051 \times 10^{23}$ (electrons/g) for the DSF-, SPC-, and SPI-based *Rh.* spp. particleboards. Since the DSF15′, SPC15′, and SPI15′ samples exhibited a wide range of atomic numbers, from carbon to zinc, compared with the other particleboard samples, they had higher N_{el}. The maximal values of N_{el} registered for the DSF15′, SPC15′, and SPI15′ samples suggest their preferable radiation shielding effectiveness compared with the other studied particleboards. Therefore, the presence and symmetrical distribution of DSF15′,

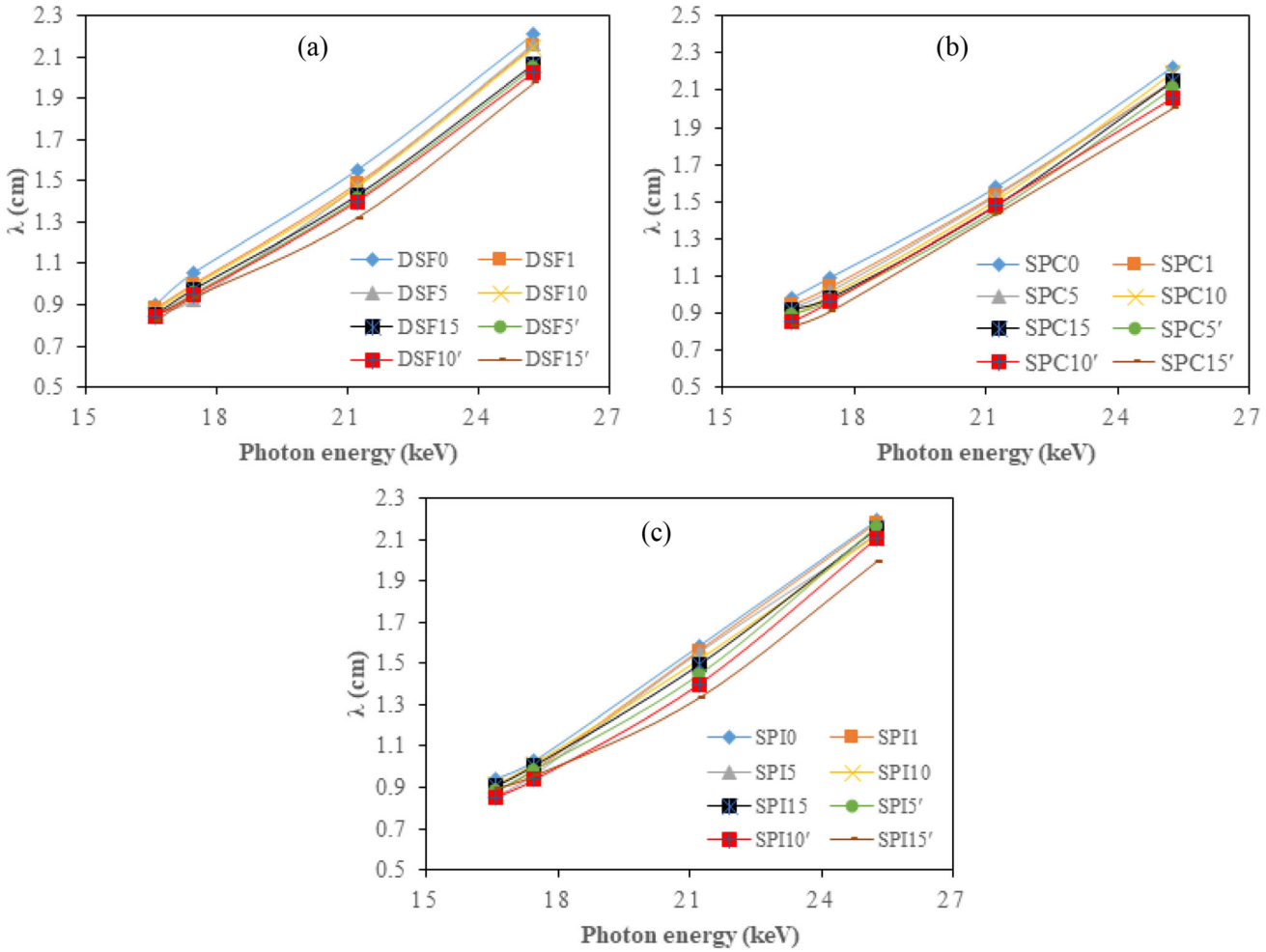

Fig. 10 (Color online) Calculated MFPs versus photon energy, for the studied particleboard samples: **a** DSF-based, **b** SPC-based, and **c** SPI-based

SPC15′, and SPI15′ with high effective electron densities increased the interaction probability between photons and the particleboard composites.

3.5 HVL, TVL, and MFP values of the DSF-, SPC-, SPI/NaOH/IA-PAE/*Rh.* spp. particleboards

Figure 8a–c show the HVL ($X_{1/2}$), while Fig. 9a–c illustrate the TVL ($X_{1/10}$) of the DSF-, SPC-, and SPI/NaOH/IA-PAE/*Rh.* spp. particleboard samples. From these figures, it is clear that HVL and TVL are affected by the chemical contents of the particleboard samples as well as by the incident photon energy. Furthermore, with increasing the incident photon energy, the HVL and TVL values for all of the studied particleboard samples increase rapidly and reach maxima at 25.26 keV. This can be attributed to the dominance of the photon interaction process, which in this range of energies is the photoelectric effect [8, 17, 19, 21, 23]. These results indicate that as the energy increases, energetic photons are more likely to penetrate their target medium. It is worth noting that with increasing the IA-PAE concentration, the variations of the HVL and TVL become identical, and the only difference is in the magnitudes of the HVL and TVL. Moreover, it is clear that DSF15′, SPC15′, and SPI15′ have the lowest HVL and TVL values, which can be explained by a steady increase in the density (Table 1) and an increase in the mass attenuation coefficients (Table 2). This can also be ascribed to the more significant presence of high-atomic-number elements in the samples. This suggests more photon interactions with DSF15′, SPC15′, and SPI15′, which ensures more effective radiation shielding. Figure 10a–c show the dependence of MFP (λ) on the photon energy, for the DSF-, SPC-, and SPI-based *Rh.* spp. particleboards. Evidently, MFP is high for the samples with low Z_{eff} and N_{el}. On the other hand, for the samples with higher Z_{eff} and N_{el}, the MFP values are relatively small. Evidently, MFP varies significantly across the particleboard samples as the

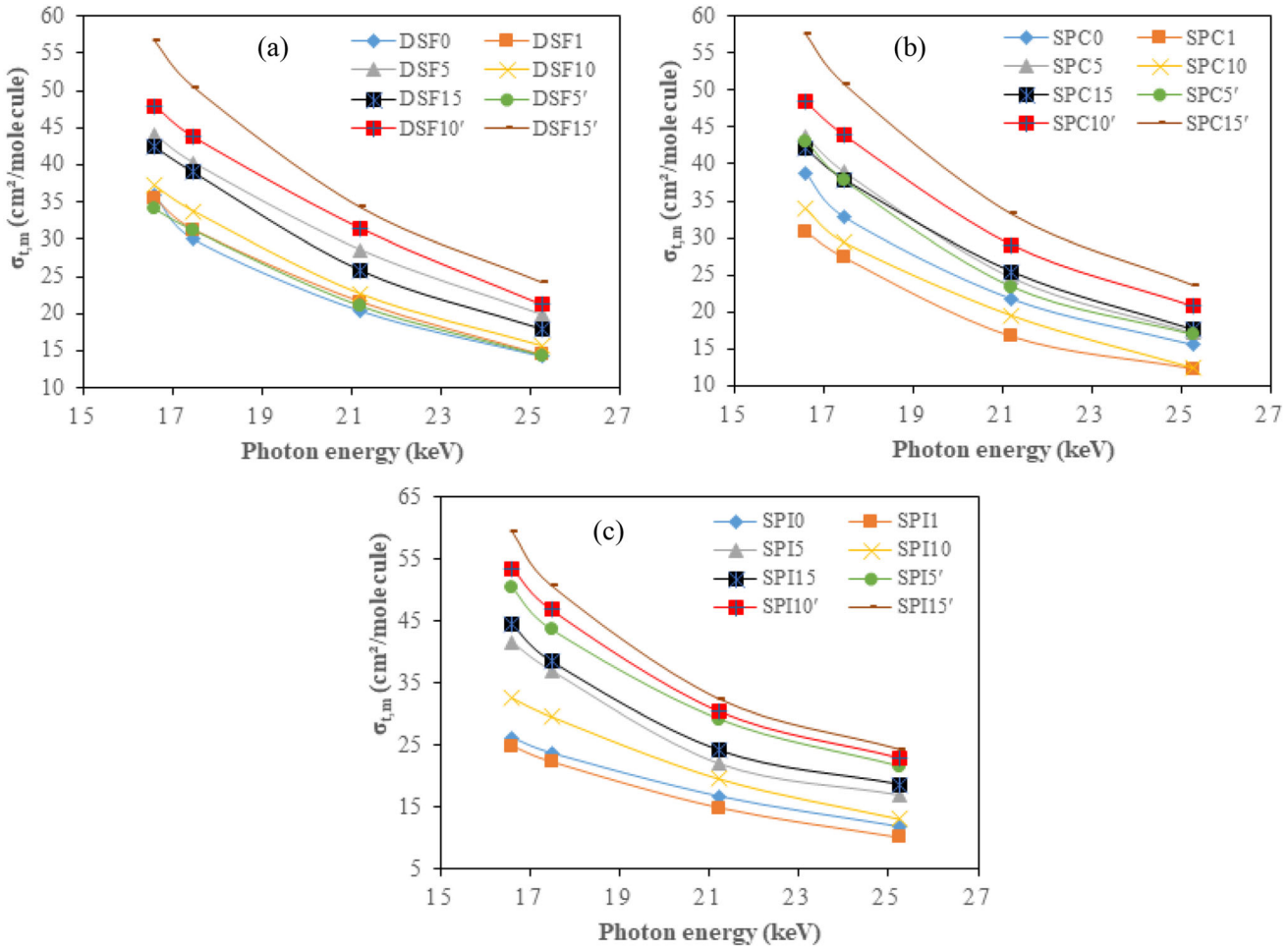

Fig. 11 (Color online) Total molecular cross section versus the photon energy, for the studied particleboard samples: **a** DSF-based, **b** SPC-based, and **c** SPI-based

photon energy increases from 16.59 keV to 25.26 keV. According to this figure, DSF15′, SPC15′, and SPI15′ have the lowest MFP values, which validates our hypothesis that adding NaOH/IA-PAE improved the radiation shielding properties of the DSF-, SPC-, SPI/NaOH/IA-PAE/*Rh.* spp. particleboard samples. However, it should be pointed out that DSF0, SPC0, and SPI0 have the highest MFP values among all of the studied particleboard samples, followed closely by DSF1, SPC1, and SPI1. It was revealed that DSF15′, SPC15′, and SPI15′ samples with the lowest values of HVL, TVL, and MFP appear to be better materials for reducing the radiation intensity, suggesting that these materials have good shielding characteristics.

3.6 Total molecular, effective atomic, and electronic cross sections of the DSF-, SPC-, and SPI/NaOH/IA-PAE/*Rh.* spp. particleboards

The energy dependence of the computed $\sigma_{t,m}$, $\sigma_{t,a}$, and $\sigma_{t,el}$ is displayed in Figs. 11a–c, 12a–c, and 13a–c, respectively. It is worth noting from Figs. 11a–c and 12a–c that there is a certain variation in the values of $\sigma_{t,m}$ and $\sigma_{t,a}$, but as the photon energy increases, the values decrease exponentially. It can be clearly seen Fig. 13a–c that the SPC0, DSF5, SPC5, SPI5, DSF10, DSF15, SPC15, and SPI15 samples have higher $\sigma_{t,el}$ compared with the other particleboard samples, but the values drop sharply with increasing photon energy. Moreover, the values of these parameters decrease with increasing the number of elements in the particleboard samples. DSF15′, SPC15′, and SPI15′, which contain the 15 wt% IA-PAE (highest value), exhibit the highest $\sigma_{t,m}$. The highest values of $\sigma_{t,a}$ are observed for DSF15, SPC15, and SPI15. In contrast, the DSF15′, SPC15′, and SPI15′ samples exhibit the lowest $\sigma_{t,el}$ values compared with the other selected samples. From these results, it can be concluded that DSF-, SPC-, and SPI/NaOH/IA-PAE/*Rh.* spp. particleboards have appropriate shielding characteristics, and are likely to be beneficial in medical health applications.

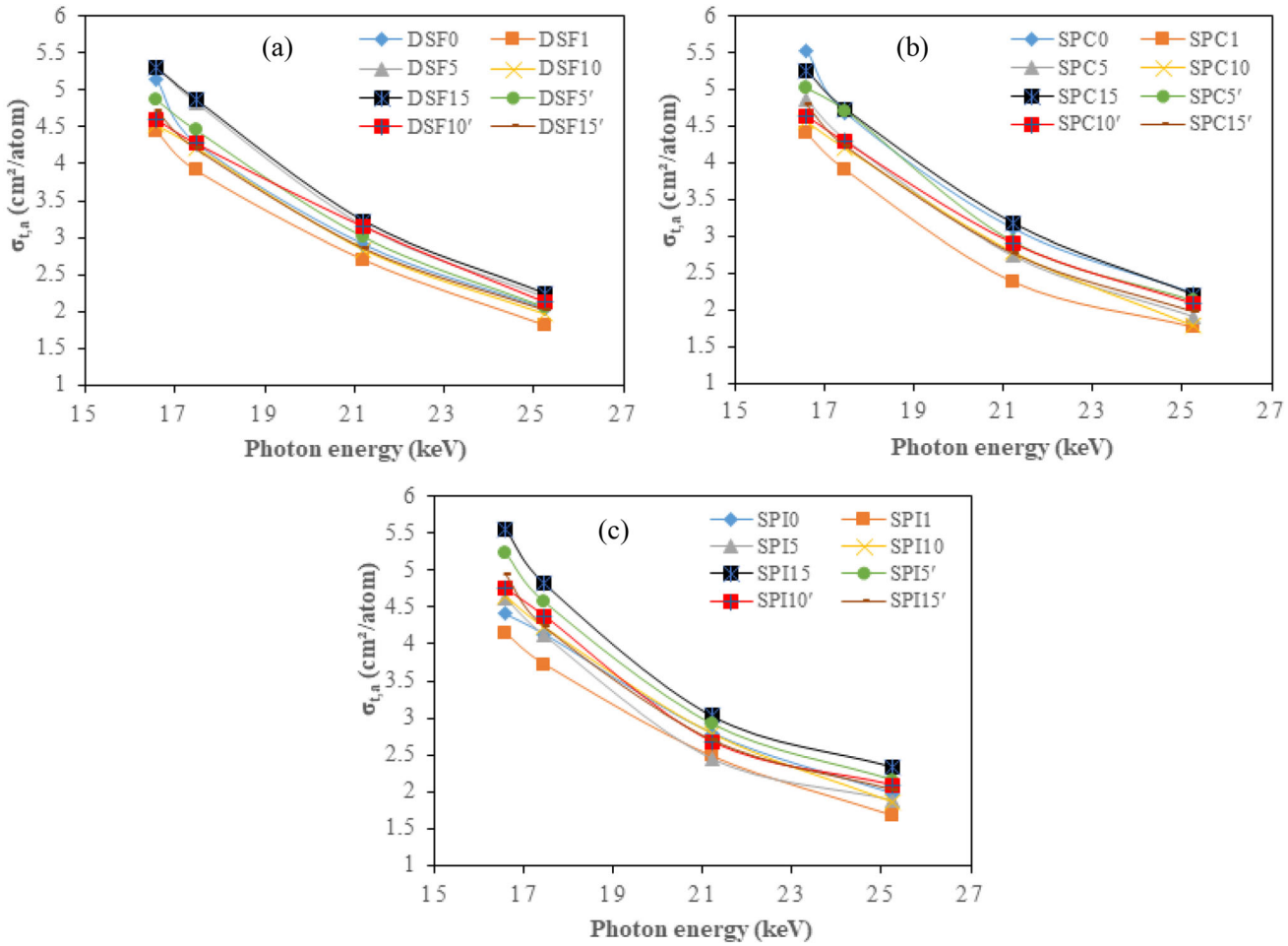

Fig. 12 (Color online) Total effective atomic cross sections versus the photon energy, for the studied particleboard samples: **a** DSF-based, **b** SPC-based, and **c** SPI-based

4 Conclusion

In the present work, we determined the radiation attenuation parameters of DSF-, SPC-, and SPI/NaOH/IA-PAE/*Rh.* spp. particleboards with respect to low-energy X-ray interactions in the 16.59–25.26 keV range. All of the studied particleboard samples were amorphous, which was validated by XRD. The micrograph images of the studied DSF15′, SPC15′, and SPI15′ particleboards revealed enhancement in terms of compactness and the number of void spaces, compared with the uncured samples. The radiation attenuation parameters depended on the particleboard composition, photon energy, and concentration of NaOH/IA-PAE modifiers. The DSF15′, SPC15′, and SPI15′ particleboards had the highest values of μ_m, ε, Z_{eff}, and N_{el}, while the HVL, TVL, and MFP values of these particleboards were the lowest among the other particleboards. These particleboard samples also exhibited the highest values of $\sigma_{t,m}$ and the smallest values of $\sigma_{t,a}$ and $\sigma_{t,el}$, respectively. These observations suggested that NaOH/IA-PAE significantly affected the photon attenuation characteristics of the DSF-, SPC-, and SPI-based *Rh.* spp. particleboards. The presently reported results suggest that DSF-, SPC-, and SPI/NaOH/IA-PAE/*Rh.* spp. particleboards with 15 wt% IA-PAE can be used as radiation shielding materials in medical health applications.

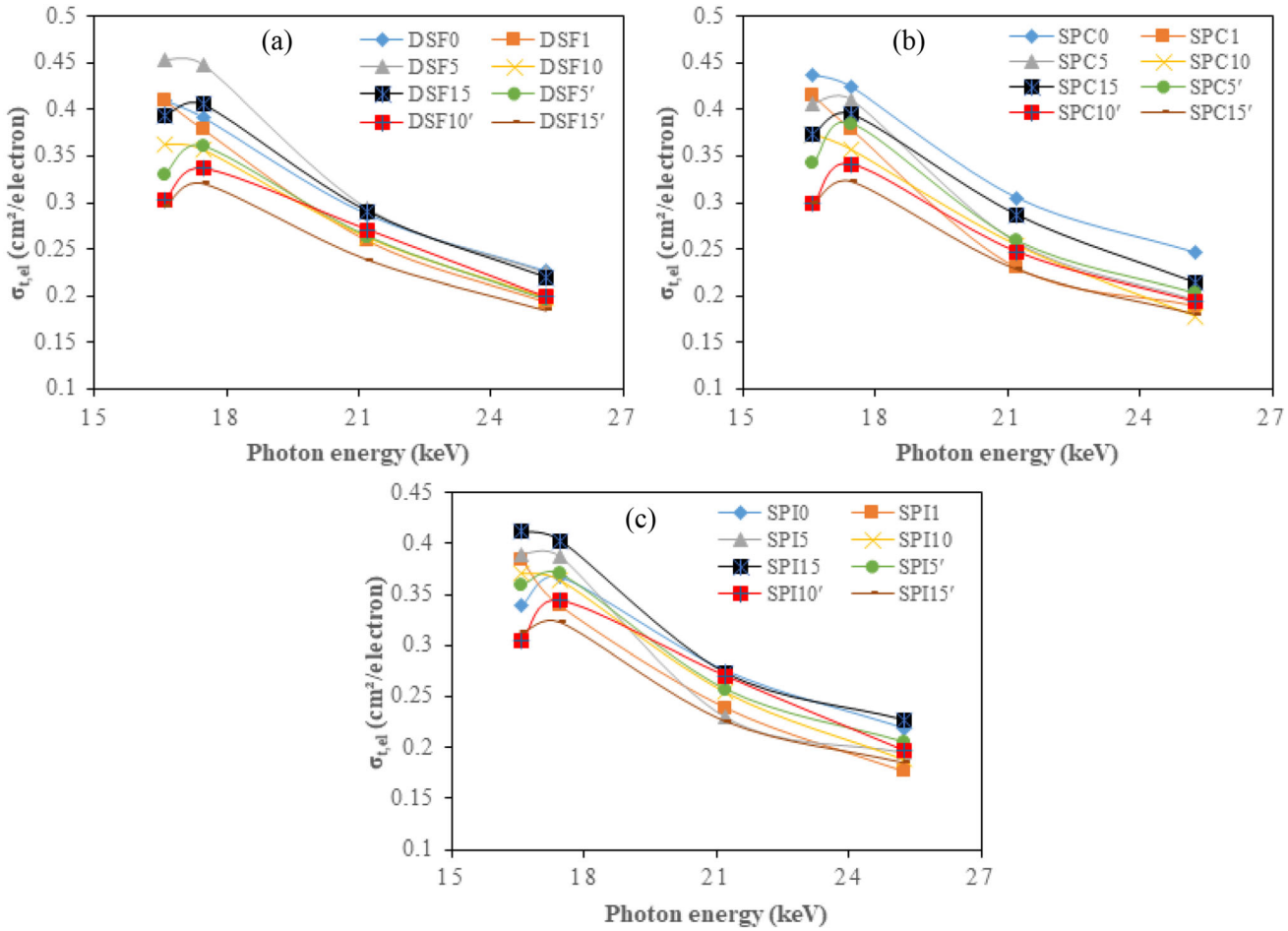

Fig. 13 (Color online) Comparison of total electronic cross sections versus the photon energy, for the studied particleboard samples

Author contributions All authors contributed to the study conception and design. Material preparation, data collection, and analysis were performed by Damilola Oluwafemi Samson, Ahmad Shukri, Mohd Zubir Mat Jafri, Rokiah Hashim, Mohd Zahri Abdul Aziz, Sylvester Jande Gemanam, and Mohd Fahmi Mohd Yusof. The first draft of the manuscript was written by Damilola Oluwafemi Samson and all authors commented on previous versions of the manuscript. All authors read and approved the final manuscript.

References

1. V.P. Singh, N.M. Badiger, N. Kucuk, Assessment of methods for estimation of effective atomic numbers of common human organs and tissue substitutes: waxes, plastics and polymers. Radioprotection **49**(2), 115–121 (2014). https://doi.org/10.1051/radiopro/2013090
2. M. Dong, X. Xue, S. Liu et al., Using iron concentrate in Liaoning Province, China, to prepare material for X-ray shielding. J. Cleaner. Prod. **210**, 653–659 (2019). https://doi.org/10.1016/j.jclepro.2018.11.038
3. M. Jamil, M.H. Hazlan, R.M. Ramli et al., Study of electrospun PVA-based concentrations nanofibre filled with Bi_2O_3 or WO_3 as potential X-ray shielding material. Radiat. Phys. Chem. **156**, 272–282 (2019). https://doi.org/10.1016/j.radphyschem.2018.11.018
4. M.H. Shannon, A.C. Katherine, Is lead dust within nuclear medicine departments a hazard to pediatric patients? J. Nucl. Med. Technol. **37**(3), 170–172 (2009). https://doi.org/10.2967/jnmt.109.062281
5. S.N.A. Abdullah, Incorporation of metals into *Rhizohora* spp. binderless particleboard as a material for radiation shielding. M.Sc. Thesis, Universiti Sains Malaysia (USM), Malaysia (2014)
6. Y. Elmahroug, B. Tellili, C. Souga, Determination of shielding parameters for different types of resins. Ann. Nucl. Energy **63**, 619–623 (2014). https://doi.org/10.1016/j.anucene.2013.09.007
7. H. Alavian, H. Tavakoli-Anbaran, Study on gamma shielding polymer composites reinforced with different sizes and proportions of tungsten particles using MCNP code. Prog. Nucl. Energy **115**, 91–98 (2019). https://doi.org/10.1016/j.pnucene.2019.03.033
8. D.O. Samson, M.Z. Mat Jafri, A. Shukri et al., Measurement of radiation attenuation parameters of modified defatted soy flour–soy protein isolate-based mangrove wood particleboards to be used for CT phantom production. Radiat. Environ. Biophys. **59**(3), 493–501 (2020). https://doi.org/10.1007/s00411-020-00844-z
9. A.A. Tajuddin, C.W.A.C.W. Sudin, D.A. , Bradley, Radiographic and scattering investigation on the suitability of *Rhizophora* spp. as tissue-equivalent medium for dosimetric study. Radiat. Phys. Chem. **47**(5), 739–740 (1996). https://doi.org/10.1016/0969-806X(95)00052-Y

10. M.A. Anugrah, S. Suryani, S. Ilyas et al., Composite gelatin/*Rhizophora* spp. particleboards/PVA for soft tissue phantom applications. Radiat. Phys. Chem. **173**, 108878 (2020). https://doi.org/10.1016/j.radphyschem.2020.108878
11. B. Ababneh, A.A. Tajuddin, R. Hashim et al., Investigation of mass attenuation coefficient of almond gum bonded *Rhizophora* spp. particleboard as equivalent human tissue using XRF technique in the 16.6–25.3 keV photon energy. Austral. Phys. Eng. Sci. Med. **39**(4), 871–876 (2016). https://doi.org/10.1007/s13246-0482-6
12. D.A. Bradley, A.A. Tajuddin, C.W.A.C.W. Sudin et al., Photon attenuation studies on tropical hardwoods. Int. J. Radiat. Appl. Instrum. Part A Appl. Radiat. Isotopes **42**(8), 771–773 (1991). https://doi.org/10.1016/0883-2889(91)90182-Z
13. Z. He, *Bio-Based Wood Adhesives-Preparation, Characterization and Testing* (CRC Press, Boca Raton, 2017).
14. C. Gui, G. Wang, D. Wu et al., Synthesis of a bio-based polyamidoamine-epichlorohydrin resin and its application for soy-based adhesives. Int. J. Adhes. Adhes. **44**, 237–242 (2013). https://doi.org/10.1016/j.ijadhadh.2013.03.011
15. X. Zhang, Y. Zhu, Y. Yu et al., Improve performance of soy flour-based adhesive with a lignin-based resin. Polyms. **9**(7), 261 (2017). https://doi.org/10.3390/polym9070261
16. A.M. Madbouly, E.R. Atta, Comparative study between lead oxide and lead nitrate polymer as gamma—radiation shielding materials. J. Environ. Prot. **7**, 268–276 (2016). https://doi.org/10.4236/jep.2016.72023
17. P.S. Kore, P.P. Pawar, Measurements of mass attenuation coefficient, effective atomic number and electron density of some amino acids. Radiat. Phys. Chem. **98**, 86–91 (2014). https://doi.org/10.1016/j.radphyschem.2013.12.038
18. B. Aktas, S. Yalcin, K. Dogru et al., Structural and radiation shielding properties of chromium oxide doped borosilicate glass. Radiat Phys. Chem. **156**, 144–149 (2019). https://doi.org/10.1016/j.radphyschem.2018.11.012
19. A. Tursucu, D. Demir, P. Önder, Effective atomic number determination of rare earth oxides with scattering intensity ratio. Sci. Tech. Nucl. Inst., 1–6 (2013). https://doi.org/10.1155/2013/738978
20. S.R. Manohara, S.M. Hanagodimath, K.S. Thind et al., On the effective atomic number and electron density: A comprehensive set of formulas for all types of materials and energies above 1 keV. Nucl. Instrum. Methods Phys. Res. Sect. B Beam. Interact. Mater. Atoms **266**(18), 3906–3912 (2008). https://doi.org/10.1016/j.nimb.2008.06.034
21. C. Eke, O. Agar, C. Segebade et al., Attenuation properties of radiation shielding materials such as granite and marble against γ-ray energies between 80 and 1350 keV. Radiochim. Acta **105**(10), 851–863 (2017). https://doi.org/10.1515/ract-2016-2690
22. M.G. Dong, O. Agar, H.O. Tekin et al., A comparative study on gamma photon shielding features of various germanate glass systems. Compos. Part B Eng. **165**, 636–647 (2019). https://doi.org/10.1016/j.compositesb.2019.02.022
23. M. Büyükyıldız, M.A. Taşdelen, Y. Karabul et al., Measurement of photon interaction parameters of high-performance polymers and their composites. Radiat. Effects Defects Solids **173**(5–6), 474–488 (2018). https://doi.org/10.1080/10420150.2018.1477155
24. J. Wu, Q. Sun, H. Huang et al., Enhanced physico-mechanical, barrier and antifungal properties of soy protein isolate film by incorporating both plant-sourced cinnamaldehyde and facile synthesized zinc oxide nanosheets. Colloids Surf. B Biointerfaces **180**, 31–38 (2019). https://doi.org/10.1016/j.colsurfb.2019.04.041
25. E.W. Michael, H. Norman, B.C. Tyler et al., Atomic weights of the elements 2011 (IUPAC Technical Report). Pure Appl. Chem. **85**(5), 1047–1078 (2013). https://doi.org/10.1351/PAC-REP-13-03-02
26. V. Trunova, A. Sidorina, V. Kriventsov, Measurement of X-ray mass attenuation coefficients in biological and geological samples in the energy range of 7–12 keV. Appl. Radiat. Isotopes **95**, 48–52 (2015). https://doi.org/10.1016/j.apradiso.2014.09.017
27. B.T. Tonguc, H. Arslana, M.S. Al-Buriahia, Studies on mass attenuation coefficients, effective atomic numbers and electron densities for some biomolecules. Radiat Phys. Chem. **153**, 86–91 (2018). https://doi.org/10.1016/j.radphyschem.2018.08.025
28. A. Aşkın, M.I. Sayyed, A. Sharma et al., Investigation of the gamma ray shielding parameters of (100–x) [0.5Li_2O–0.1B_2O_3–0.4P_2O_5]-xTeO2 glasses using Geant4 and FLUKA codes. J. Non-Crystalline Solids **521**, 119489 (2019). https://doi.org/10.1016/j.jnoncrysol.2019.119489
29. A. Un, F. Demir, Determination of mass attenuation coefficients, effective atomic numbers and effective electron numbers for heavy-weight and normal-weight concretes. Appl. Radiat. Isot. **80**, 73–77 (2013). https://doi.org/10.1016/j.apradiso.2013.06.015
30. Y. Al-Hadeethi, M.I. Sayyed, Y.S. Rammah, Fabrication, optical, structural and gamma radiation shielding characterizations of GeO_2–PbO–Al_2O_3–CaO glasses. Ceramics Int. **46**, 2055–2062 (2020). https://doi.org/10.1016/j.ceramint.2019.09.185
31. M.I. Sayyed, F. Akman, I.H. Geçibesler et al., Measurement of mass attenuation coefficients, effective atomic numbers, and electron densities for different parts of medicinal aromatic plants in low-energy region. Nucl. Sci. Tech. **29**(144), 1–10 (2018). https://doi.org/10.1007/s41365-018-0475-0